Inorganic Chemistry

Article

pubs.acs.org/IC

Latent Porosity in Alkali-Metal $M_2B_{12}F_{12}$ Salts: Structures and Rapid Room-Temperature Hydration/Dehydration Cycles

Dmitry V. Peryshkov,*[,†,‡] Eric V. Bukovsky,*[,†] Matthew R. Lacroix,[†] Hui Wu,[§] Wei Zhou,[§] W. Matthew Jones,[†] Matic Lozinšek,[†,⊥] Travis C. Folsom,[†] D. Luke Heyliger,[†] Terrence J. Udovic,[§] and Steven H. Strauss*[,†]

[†]Department of Chemistry, Colorado State University, Fort Collins, Colorado 80523, United States

[‡]Department of Chemistry and Biochemistry, University of South Carolina, Columbia, South Carolina 29208, United States

[§]Center for Neutron Research, National Institute of Standards and Technology (NIST), Gaithersburg, Maryland 20899, United States

[⊥]Department of Inorganic Chemistry and Technology, Jožef Stefan Institute, 1000 Ljubljana, Slovenia

Supporting Information

ABSTRACT: Structures of the alkali-metal hydrates $Li_2(H_2O)_4Z$, $LiK(H_2O)_4Z$, $Na_2(H_2O)_3Z$, and $Rb_2(H_2O)_2Z$, unit cell parameters for Rb_2Z and $Rb_2(H_2O)_2Z$, and the density functional theory (DFT)-optimized structures of K_2Z, $K_2(H_2O)_2Z$, Rb_2Z, $Rb_2(H_2O)_2Z$, Cs_2Z, and $Cs_2(H_2O)Z$ are reported ($Z^{2-} = B_{12}F_{12}^{2-}$) and compared with previously reported X-ray structures of $Na_2(H_2O)_{0,4}Z$, $K_2(H_2O)_{0,2,4}Z$, and $Cs_2(H_2O)Z$. Unusually rapid room-temperature hydration/dehydration cycles of several $M_2Z/M_2(H_2O)_nZ$ salt hydrate pairs, which were studied by isothermal gravimetry, are also reported. Finely ground samples of K_2Z, Rb_2Z, and Cs_2Z, which are not microporous, exhibited latent porosity by undergoing hydration at 24–25 °C in the presence of 18 Torr of $H_2O(g)$ to $K_2(H_2O)_2Z$, $Rb_2(H_2O)_2Z$, and $Cs_2(H_2O)Z$ in 18, 40, and 16 min, respectively. These hydrates were dehydrated at 24–25 °C in dry N_2 to the original anhydrous M_2Z compounds in 61, 25, and 76 min, respectively (the exact times varied from sample to sample depending on the particle size). The hydrate $Na_2(H_2O)_2Z$ also exhibited latent porosity by undergoing multiple 90 min cycles of hydration to $Na_2(H_2O)_3Z$ and dehydration back to $Na_2(H_2O)_2Z$ at 23 °C. For the K_2Z, Rb_2Z, and Cs_2Z transformations, the maximum rate of hydration (rh_{max}) decreased, and the absolute value of the maximum rate of dehydration (rd_{max}) increased, as T increased. For $K_2Z \leftrightarrow K_2(H_2O)_2Z$ hydration/dehydration cycles with the same sample, the ratio rh_{max}/rd_{max} decreased 26 times over 8.6 °C, from 3.7 at 23.4 °C to 0.14 at 32.0 °C. For $Rb_2Z \leftrightarrow Rb_2(H_2O)_2Z$ cycles, rh_{max}/rd_{max} decreased from 0.88 at 23 °C to 0.23 at 27 °C. For $Cs_2Z \leftrightarrow Cs_2(H_2O)Z$ cycles, rh_{max}/rd_{max} decreased 20 times over 8 °C, from 6.7 at 24 °C to 0.34 at 32 °C. In addition, the reversible substitution of D_2O for H_2O in fully hydrated $Rb_2(H_2O)_2Z$ in the presence of N_2/16 Torr of $D_2O(g)$ was complete in only 60 min at 23 °C.

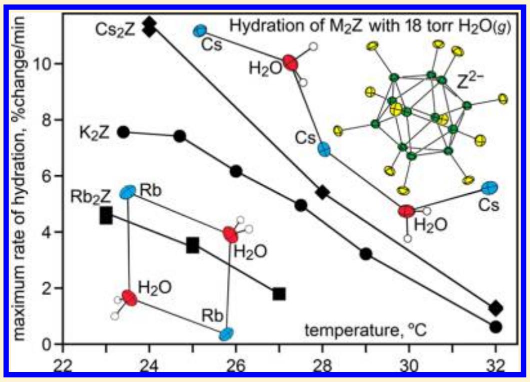

1. INTRODUCTION

We are studying anhydrous, hydrated, and solvated salts of the icosahedral superweak anion $B_{12}F_{12}^{2-}$ (hereinafter Z^{2-}).[1−8] Our interests are multifold: (i) structural changes that occur upon reversible solid-state hydration/dehydration or solvation/desolvation in the presence/absence of solvent vapor can serve as models for the solid-state diffusion of gaseous reactants and products in lattices;[9−13] (ii) thermodynamic and kinetic studies of metal salt hydration/dehydration may help to improve the efficacy of metal salt hydrate pairs used for the storage of low potential heat from solar energy (there are many thermodynamic studies but very few kinetic dehydration/rehydration studies and none at temperatures ≤32 °C);[14−17] (iii) the structures of salt hydrates can serve as models for the hydration of metal ions or metal cation−anion inner-sphere ion pairs in solution[18−21] or in extended solids such as metal−organic frameworks (MOFs)[22] and zeolites;[23−26] (iv) current interest in the superconductivity in hydrated Na_xCoO_2,[27] superionic conductivity in anhydrous $Na_2B_{12}H_{12}$,[28,29] Li^+ ion conductivity in hydrated $Li_{0.5}FeOCl$,[30] and the superior thermoelectric response of hydrated Na_xRhO_2;[31] (v) extensive dehydration/rehydration studies of pharmaceutical and antimicrobial hydrates.[32−34]

In 2010, we reported that the solid-state transformations $K_2Z + 2H_2O(g) \rightarrow K_2(H_2O)_2Z$ and $K_2(H_2O)_2Z \rightarrow K_2Z + 2H_2O(g)$ under 21 and 0 Torr of partial pressure of $H_2O(g)$ in He, respectively, required only ca. 15 and 75 min, respectively, at a constant temperature (T) of 25 °C (>98% complete reactions; samples were finely ground microcrystalline powders).[1]

Received: August 11, 2017
Published: September 21, 2017

DOI: 10.1021/acs.inorgchem.7b02081
Inorg. Chem. 2017, 56, 12023−12041

In addition, the reversible transformations $K_2(H_2O)_2Z$ + $2D_2O(g) \rightleftharpoons K_2(D_2O)_2Z + 2H_2O(g)$ were >90% complete in only 120 min at 25 °C when the partial pressure of water in the He gas stream was changed from 21 Torr of $H_2O(g)$ to 18 Torr of $D_2O(g)$ and back to 21 Torr of $H_2O(g)$. The unusually rapid and repeatable room-temperature hydration/dehydration cycles and H_2O/D_2O exchange cycles in crystalline solids that are not microporous, viz., K_2Z and $K_2(H_2O)_2Z$,[1] were termed latent porosity, which we defined as the rapid creation of space in a nonporous crystal lattice in response to the presence of reactive gases at $T = 25 \pm 5$ °C.[1] The structures of K_2Z,[2] $K_2(H_2O)_2Z$,[1] $K_2(H_2O)_4Z$,[1] and $Cs_2(H_2O)Z$[2] were reported in 2010. The structures of Na_2Z[7] and $Na_2(H_2O)_4Z$[7] were reported in 2016.

In this work, we report the dehydration and rehydration behavior of $M_2(H_2O)_nZ$ compounds of all five alkali-metal ions (n = 0−4) by isothermal and/or nonisothermal thermogravimetric analysis (TGA). This includes new results for $K_2(H_2O)_2Z \leftrightarrow K_2Z$ dehydration/rehydration cycles, the demonstration that Rb_2Z, Cs_2Z, and $Na_2(H_2O)_2Z$ also exhibit latent porosity, the temperature dependence of the rates of hydration and dehydration, and the rapid exchange of H_2O and D_2O molecules when crystalline $Rb_2(H_2O)_2Z$ is exposed to 16 Torr of $D_2O(g)$ or when $Rb_2(D_2O)_2Z$ is exposed to 18 Torr of $H_2O(g)$. We also report the single-crystal X-ray diffraction (SC-XRD) structures of $Li_2(H_2O)_4Z$, $LiK(H_2O)_4Z$, $Na_2(H_2O)_3Z$, and $Rb_2(H_2O)_2Z$, the powder X-ray diffraction (PXRD)-determined unit cell parameters for Rb_2Z and $Rb_2(H_2O)_2Z$ at room temperature, and the density functional theory (DFT)-optimized structures of K_2Z, $K_2(H_2O)_2Z$, Rb_2Z, $Rb_2(H_2O)_2Z$, Cs_2Z, and $Cs_2(H_2O)Z$. The structures support possible explanations for the unusually rapid solid-state dehydration/rehydration and H_2O/D_2O exchange reactions at room temperature. In addition, because Li_2Z has applications as an electrolyte for secondary batteries and other electrochemical devices,[35−39] we also report a method to isolate it with high-purity and minimal residual H_2O.

2. EXPERIMENTAL METHODS

Reagents and General Procedures. Anhydrous compounds were prepared using standard airless-ware glassware and a Schlenk-style vacuum line and stored in a nitrogen-filled glovebox.[40] Potassium dodecafluoro-*closo*-dodecaborate(2−), K_2Z ($Z^{2-} = B_{12}F_{12}^{\ 2-}$), was synthesized by the direct fluorination of $K_2B_{12}H_{12}$ with 80:20 N_2/F_2 in CH_3CN at 0 °C and purified as previously described.[5,41,42] [***Caution!*** *The original purification procedure*[41,42] *involving* H_2O_2 *is not recommended because of the potential isolation of explosive* $K_2(H_2O_2)_{2-x}(H_2O)_xZ$. *An alternate, safer procedure*[5] *is recommended.*] The substitution of F atoms for H atoms was monitored periodically using negative-ion electrospray-ionization mass spectrometry (NI-ESI-MS), as previously described.[41] The final degree of F/H metathesis, determined by NI-ESI-MS and $^{19}F\{^{11}B\}$ and $^{11}B\{^{19}F\}$ NMR spectroscopy as previously described,[41] was found to be 99.5+%. Recrystallization from water removed a trace amount of BF_4^- that was present. It is important to remove BF_4^- contamination from the potassium salt because it was not possible to efficiently remove BF_4^- from either Li_2Z or Na_2Z by recrystallization. The hydrated salts $Na_2(H_2O)_4Z$[7] and $Cs_2(H_2O)Z$[2] and the solvated salt $Ag_2(CH_3CN)_4Z$[43,44] were prepared as previously described. Distilled water was deionized with a Barnstead Nanopure system. The deionized distilled water (dd-H_2O) had a resistivity greater than or equal to 18 MΩ (all samples of H_2O used in this work correspond to dd-H_2O prepared in this way). The following reagents were obtained from the indicated suppliers and used as received: deuterium oxide (D_2O, Cambridge Isotopes, 99.9% D); LiCl (Mallinckrodt, ACS reagent grade, lot G21621); RbCl (K&K, 99%). [The mention of all commercial suppliers in this paper is for clarity. This does not imply the recommendation or endorsement of these suppliers by NIST.]

High-Purity Anhydrous Li_2Z and $Li_2(H_2O)_4Z$. An aqueous solution of K_2Z was converted to Li_2Z using the cation-exchange resin Purolite UCW 9126. The ion-exchange column was prepared using a 10 wt % aqueous solution of ACS reagent-grade LiCl, the specifications for which list the maximum amounts of K^+ and Na^+ as 0.01 and 0.02 mol %, respectively. The completeness of Li^+/K^+ cation exchange was determined by inductively coupled plasma atomic emission spectroscopy (ICP-AES; see below). After a single pass through the cation-exchange column, the lithium salt contained 0.06 mol % K^+, 0.27 mol % Na^+, and 99.57 mol % Li^+. Small amounts of Cu^{2+} (0.02 mol %) and Mg^{2+} (0.05 mol %) were also detected. The specifications for ACS-reagent-grade LiCl do not list these metal ions. All other metal ions that were measured by ICP-AES were less than 0.01 mol % (these were Ag, Al, As, Au, B, Ba, Be, Ca, Cd, Ce, Co, Cr, Cu, Fe, K, Li, Mg, Mn, Mo, Na, Ni, P, Pb, Pd, Pt, S, Sb, Se, Si, Sn, Sr, Te, Ti, Tl, U, V, W, Zn, and Zr). An aqueous solution of the lithium salt was passed through a freshly lithium-regenerated column and reduced the amount of K^+ to less than 0.01 mol %. Anhydrous $Li_2(B_{12}F_{12})$, which is hygroscopic when exposed to air, was isolated from the purified aqueous solution by rotary evaporation, followed by heating at 175−180 °C under vacuum for 24 h. The range of yields of anhydrous Li_2Z from several syntheses was 85−90% based on the K_2Z starting material. Recrystallization from water afforded single crystals of $Li_2(H_2O)_4Z$ suitable for X-ray diffraction (XRD) and TGA. It is likely that the use of a higher-purity grade of LiCl would result in even less contamination with Na^+, K^+, and other metal ions.

$LiK(H_2O)_4Z$. A 50:50 mol % aqueous solution of Li_2Z and K_2Z was allowed to slowly evaporate, yielding single crystals of $LiK(H_2O)_4Z$ suitable for XRD and TGA. Optimization of the amount of crystalline $LiK(H_2O)_4Z$ isolated was not attempted, and therefore a yield was not determined.

$Na_2(H_2O)_3Z$. An aqueous solution of Na_2Z was stored over a large amount of solid $Ca(NO_3)_2$ in a desiccator at 22(1) °C [the vapor pressure of H_2O over a saturated solution of $Ca(NO_3)_2$ at 22(1) °C is 10 Torr]. Slow evaporation of the solution resulted in single crystals of $Na_2(H_2O)_3Z$ suitable for XRD and TGA. Optimization of the amount of crystalline $Na_2(H_2O)_3Z$ isolated was not attempted, and therefore a yield was not determined, in part because slight changes in this procedure sometimes resulted in the crystallization of $Na_2(H_2O)_4Z$ instead of $Na_2(H_2O)_3Z$.

$Rb_2(H_2O)_2Z$. An aqueous mixture of RbCl and $Ag_2(CH_3CN)_4Z$ was filtered to remove AgCl. Slow evaporation of the filtrate resulted in single crystals of $Rb_2(H_2O)_2Z$ suitable for XRD and TGA. Optimization of the amount of crystalline $Rb_2(H_2O)_2Z$ isolated was not attempted, and therefore a yield was not determined.

TGA. Samples for TGA (Pt sample pans; 10−15 mg of finely ground microcrystalline powders) were analyzed using TA Instruments series 2950 or TGA Q500 instrumentation. The temperatures for isothermal TGA experiments, which ranged from 23 to 32 °C, were held to within 0.01 °C for several minutes before a change in the carrier gas was made. Dry He, dry N_2 or either gas bubbled through H_2O, D_2O, or a saturated aqueous solution of NaCl was used as the carrier gas depending on the experiment. When the carrier gas was bubbled through H_2O, D_2O, or saturated NaCl(aq) at 21(1) °C, the vapor pressure of H_2O or D_2O in the sample chamber was 18(1) Torr of $H_2O(g)$, 16(1) Torr of $D_2O(g)$, or 14(1) Torr of $H_2O(g)$, respectively. Whenever the carrier gas was switched [e.g., from dry gas to a gas containing $H_2O(g)$ or from gas containing $H_2O(g)$ to gas containing $D_2O(g)$ or vice versa], ca. 0.5 min elapsed before the composition of the carrier gas in the sample chamber became constant, as monitored in several control experiments by recording the mass spectrum of the carrier gas exiting the sample chamber (see Figures S1 and S2, which are reproduced from ref 1). The carrier gas flow rate was 60 mL min^{-1}.

ICP-AES. Metal analyses were performed using PerkinElmer model 7300 DV ICP-OES and ICP-AES instruments. Elements analyzed were Ag, Al, As, Au, B, Ba, Be, Ca, Cd, Ce, Co, Cr, Cu, Fe, K, Li, Mg, Mn, Mo, Na, Ni, P, Pb, Pd, Pt, S, Sb, Se, Si, Sn, Sr, Te, Ti, Tl, U, V,

DOI: 10.1021/acs.inorgchem.7b02081
Inorg. Chem. 2017, 56, 12023−12041

Table 1. Crystal Data and Final Refinement Parameters for the Single-Crystal X-ray Structures Reported in This Work[a]

compound	$Li_2(H_2O)_4(B_{12}F_{12})$	$LiK(H_2O)_4(B_{12}F_{12})$	$Na_2(H_2O)_3(B_{12}F_{12})$	$Rb_2(H_2O)_2(B_{12}F_{12})$
formula	$B_{12}F_{12}H_8Li_2O_4$	$B_{12}F_{12}H_8KLiO_4$	$B_{12}F_{12}H_6Na_2O_3$	$B_{12}F_{12}H_4O_2Rb_2$
fw, g mol^{-1}	443.66	475.82	457.75	564.69
cryst syst	orthorhombic	tetragonal	orthorhombic	monoclinic
space group, Z	*Ibam*, 4	$P4_2/ncm$, 4	$P2_12_12_1$, 4	$P2_1/c$, 2
a, Å	10.3005(11)	10.5921(5)	10.2974(6)	7.8511(3)
b, Å	10.3100(13)	10.5921(5)	10.3442(6)	10.2749(4)
c, Å	13.5337(13)	14.0638(9)	14.1466(9)	9.9917(4)
α, deg	90	90	90	90
β, deg	90	90	90	108.775(1)
γ, deg	90	90	90	90
V, $Å^3$	1437.3(3)	1577.9(2)	1506.9(2)	763.13(5)[c]
ρ_{calc} g cm^{-3}	2.050	2.003	2.018	2.457
T, K	120(2)	120(2)	130(2)	120(2)
$R(F)$ $[I > 2\sigma(I)]$[b]	0.0295	0.0463	0.0339	0.0184
$wR(F^2)$ (all data)[b]	0.1488	0.1694	0.0910	0.0422
GOF	1.343	1.205	1.067	1.051

[a]The radiation used was 0.71073 Å X-rays. [b]$R(F) = \sum||F_o| - |F_c||/\sum|F_o|$; $wR(F^2) = (\sum[w(F_o^2 - F_c^2)^2]/\sum[w(F_o^2)^2])^{1/2}$. [c]The unit cell volume at 297 K, determined by PXRD, is 783.2(1) $Å^3$, 2.6% larger.

W, Zn, and Zr. Samples were diluted in a mixture of metal-free acids [1% (v/v) HCl and 5% (v/v) HNO_3] to a known concentration, and the reported values were an average of three replicate measurements. Y was used as an internal standard, and 15 interelement standards were used to correct for easily ionizable elements.

SC-XRD. Data sets were collected using a Bruker Kappa APEX II CCD diffractometer, and structures were solved using standard Bruker X-ray software. Table 1 lists relevant data collection and refinement results for the four new SC-XRD structures. Tables 2 and 3 lists relevant interatomic distances and angles for the new structures and, for comparison, the previously published structures of Na_2Z,[7] $Na_2(H_2O)_4Z$,[7] $Ag_2(H_2O)_4Z$,[45] K_2Z,[2] $K_2(H_2O)_2Z$,[1] $K_2(H_2O)_4Z$,[1] and $Cs_2(H_2O)Z$,[2] including distances involving the B_{12} centroids, hereinafter denoted with the symbol ⊙. Table S-1 lists the bond-valence parameters used in this work.[46]

PXRD. Powder patterns for samples of Rb_2Z and $Rb_2(H_2O)_2Z$ in sealed quartz capillaries were collected at 24 °C using a Rigaku Ultima III powder X-ray diffractometer with Cu Kα radiation. XRD patterns and Le Bail refinement fits to the patterns for polycrystalline samples of anhydrous Rb_2Z and for $Rb_2(H_2O)_2Z$ are shown in Figure S3. Indexing of the PXRD pattern for Rb_2Z revealed that it is isomorphous with K_2Z (space group $C2/c$). The lattice parameters determined from the Le Bail refinement for Rb_2Z are a = 8.418(1) Å, b = 14.704(2) Å, c = 11.610(2) Å, β = 93.054(7)°, Z = 4, and V = 1435.1(5) $Å^3$. Indexing of the PXRD pattern for $Rb_2(H_2O)_2Z$ was consistent with the $P2_1/c$ SC-XRD structure determined at 120 K. The lattice parameters determined from the Le Bail refinement for $Rb_2(H_2O)_2Z$ are a = 7.9109(4) Å, b = 10.3972(6) Å, c = 10.0599(5) Å, β = 108.831(2)°, Z = 2, and V = 783.2(1) $Å^3$.

DFT Calculations. First-principles calculations were performed for K_2Z, $K_2(H_2O)_2Z$, Rb_2Z, $Rb_2(H_2O)_2Z$, Cs_2Z, and $Cs_2(H_2O)Z$ within the plane-wave implementation of the generalized gradient approximation to DFT using a Vanderbilt-type ultrasoft potential with Perdew–Burke–Ernzerhof (PBE) exchange correlation.[47] A cutoff energy of 544 eV and a 2 × 2 × 2 k-point mesh (generated using the Monkhorst–Pack scheme) were used and found to be enough for the total energy to converge to within 0.01 meV $atom^{-1}$. Unit cell parameters, fractional coordinates, bond distances, and bond valences for DFT K_2Z and $K_2(H_2O)_2Z$, bond distances and bond valences for SC-XRD K_2Z and $K_2(H_2O)_2Z$, and selected distances and volumes for the DFT and SC-XRD structures of K_2Z and $K_2(H_2O)_2Z$ are listed in Tables S2–S8. Unit cell parameters, fractional coordinates, bond distances, and bond valences for Rb_2Z, $Rb_2(H_2O)_2Z$, Cs_2Z, and $Cs_2(H_2O)Z$ and bond distances and bond valences for SC-XRD $Rb_2(H_2O)_2Z$ and $Cs_2(H_2O)Z$ are listed in Tables S9–S18. Selected distances and volumes are listed in Table 3.

3. RESULTS AND DISCUSSION

I. Attempts to Crystallize Mixed-Cation Salts. Crystalline salts containing both K^+ and Cs^+ are known, including $KCs(ClO_4)_2$,[48] $KCs(Pd(NO_3)_4)\cdot 0.5H_2O$,[49] and $KCs_2(Bi(SCN)_6)$.[50] However, an aqueous solution containing K^+, Cs^+, and Z^{2-} deposited crystals of the sparingly soluble salt $Cs_2(H_2O)Z$, not $KCs(H_2O)_nZ$ ($Z^{2-} = B_{12}F_{12}^{2-}$). This may be because the structures of $Cs_2(H_2O)Z$[2] and both $K_2(H_2O)_2Z$[1] and $K_2(H_2O)_4Z$[1] are substantially different. Nevertheless, an aqueous solution containing Li^+, K^+, and Z^{2-} deposited crystals of the hydrated mixed-cation salt $LiK(H_2O)_4Z$ in spite of the substantial differences between the structures of $Li_2(H_2O)_4Z$, $LiK(H_2O)_4Z$, and $K_2(H_2O)_4Z$, as discussed below. Some other mixed-cation salts containing Li^+ and a different alkali-metal ion are $LiCsTiF_6$,[51] $LiK(BH_4)_2$,[52] $LiK(N(CN)_2)_2$,[53] $LiRb(N(CN)_2)_2$,[53] and $LiK_2(SCN)_3$.[54] Two salts containing Na^+ and K^+ are $NaKSiF_6$[55] and $Na_2K_2P_2O_6\cdot 8H_2O$.[56] There are a number of other examples with octahedral MF_6^{n-} and related fluoroanions.[57] No mixed-cation salts of Z^{2-} other than $LiK(H_2O)_4Z$ have been reported.

II. New $M_2(H_2O)_nZ$ Structures. *II.A. General Comments.* Relevant interatomic distances, B_{12} centroid···centroid (⊙···⊙) distances, sums of the M–O and M–F bond valences ($\sum$bv values), and formula unit volumes are listed in Table 2 for the SC-XRD structures of $Li_2(H_2O)_4Z$, $Na_2(H_2O)_3Z$, $Na_2(H_2O)_4Z$,[7] $LiK(H_2O)_4Z$, $K_2(H_2O)_4Z$,[1] and $Ag_2(H_2O)_4Z$[45] and in Table 3 for the SC-XRD structures of $K_2(H_2O)_2Z$,[1] $Rb_2(H_2O)_2Z$, and $Cs_2(H_2O)Z$[2] and the DFT-optimized structures of Rb_2Z, $Rb_2(H_2O)_2Z$, Cs_2Z, and $Cs_2(H_2O)Z$. As expected, distances and angles within the icosahedral Z^{2-} anions in all of the structures are essentially the same and will not be discussed further. A recent review lists metal-ion and NH_4^+ salts of $B_{12}X_{12}^{2-}$ anions that were known at the end of 2015 (X = H, F, Cl, Br, I).[58] In addition to the new SC-XRD structures of Z^{2-} reported in this paper, the SC-XRD structures of $K_2(SO_2)_6Z$, $Ag_2(SO_2)_6Z$, $Ag_2(H_2O)_4Z$, $Ag_2(CH_3CN)_{4,5,8}Z$, $Ag_2(CH_2Cl_2)_4Z$, $Ag_2(C_6H_5CH_3)_6Z$, Na_2Z, $Na_2(H_2O)_4Z$, $Na_2(B_{12}Cl_{12})$, $Na_2(H_2O)_6(B_{12}Cl_{12})$, and PPh_4^+ salts of $B_{12}X_{11}(OR)^{2-}$ anions (X = Cl, Br; R = H, n-Pr, n-Oc) were also reported since 2015.[7,43,45,59]

II.B. $Li_2(H_2O)_4Z$. The structure of this compound, shown in Figures 1 and S4 and S5, is unlike the structures of any of the other hydrated alkali-metal and silver salts of Z^{2-}. The B_{12}

Table 2. Selected Interatomic Distances (Å) and Bond Valence Values for Single-Crystal X-ray Structures[a]

compound	$Li_2(H_2O)_4Z$	$Na_2(H_2O)_3Z$	$Na_2(H_2O)_4Z$[b]	$LiK(H_2O)_4Z$	$K_2(H_2O)_4Z$[c]	$Ag_2(H_2O)_4Z$[d]
M coordination sphere	LiO_2F_4	*cis*- and *trans*-NaO_2F_4[e]	NaO_4F_2	LiO_4; KO_4F_4	KO_3F_5	AgO_4F_2
M−F(B)	2.109(1) (×2), 2.118(1) (×2)	2.267(2)−2.293(2) (Na1); 2.292(2)−2.636(2) (Na2)	2.313(8)−2.381(7)	2.632(2) (×4) (K)	2.6501(6)−3.2843(7)	2.734(4)−3.021(4)
M−O	1.995(1) (×2) (K)	2.402(2), 2.434(2) (Na1); 2.387(2), 2.416(2) (Na2)	2.368(9)−2.473(9)	1.945(3) (×4) (Li); 2.856(3) (×4) (K)	2.6685(7)−2.8306(8)	2.371(4)−2.524(4)
∑bv(M−F/O)	1.00	1.16 (Na1); 1.04 (Na2)	1.01−1.14	1.10 (Li); 1.27 (K)	1.09 (K1); 1.03 (K2)	0.87 (Ag1); 0.90 (Ag2)
∑bv(M−F)	0.52	0.78 (Na1); 0.64 (Na2)	0.28−0.34	0.70 (K)	0.55 (K1); 0.49 (K2)	0.12 (Ag1); 0.16 (Ag2)
∑bv(M−O)	0.48	0.38 (Na1); 0.40 (Na2)	0.73−0.79	1.10 (Li); 0.56 (K)	0.54 (K1); 0.55 (K2)	0.75 (Ag1); 0.74 (Ag2)
M···⊙	4.972	5.119 (Na1); 4.645 (Na2)	5.037−6.303	5.843 × 4 (Li); 5.399 (×4) (K)	5.192−5.930	5.159−6.041 (Ag1); 5.117−5.959 (Ag2)
anion packing	tetragonal	distorted CsCl	offset hexagonal[f]	offset hexagonal[f]	distorted CsCl	offset hexagonal[f]
⊙···⊙	6.767, 7.287 (×2)	7.185−7.475	6.888−8.798	7.032−8.971	6.915−9.126	7.003−8.429
closest M···M	5.150(1)	4.229(1)	3.558(6)−3.609(6)	3.516(1) (Li···K)	4.3188(4)	3.540(2)

[a] $Z^{2-} = B_{12}F_{12}^{2-}$. All results are from this work unless otherwise indicated. [b] Reference 7. [c] Reference 1. [d] Reference 45. [e] Na1 has a *trans*-NaO_2F_4 coordination sphere; Na2 has a *cis*-NaO_2F_4 coordination sphere. [f] ADAD... packing (see the Supporting Information for more details).

Table 3. Selected Interatomic Distances (Å) and Bond Valence Values[a]

compound	$Rb_2(H_2O)_2Z$ SC-XRD	$Rb_2(H_2O)_2Z$ DFT	Rb_2Z DFT	$Cs_2(H_2O)Z$ SC-XRD[c]	$Cs_2(H_2O)Z$ DFT	Cs_2Z DFT	$K_2(H_2O)_2Z$[b] SC-XRD	K_2Z[c] SC-XRD
M coordination sphere	RbO_2F_8	RbO_2F_8	RbF_8 (Rb1); RbF_8 (Rb2)	CsF_{11} (Cs1); CsO_2F_7 (Cs2)	CsF_{11} (Cs1); CsO_2F_7 (Cs2)	CsF_{10} (Cs1); CsF_8 (Cs2)	KO_2F_6	KF_8 (K1); KF_8 (K2)
M−F(B)	2.91−3.24	2.94−3.35	2.81−3.00 (Rb1); 2.84−3.44 (Rb2)	3.05−3.44 (Cs1); 3.07−3.47 (Cs2)	3.13−3.42 (Cs1); 3.15−3.51 (Cs2)	3.15−3.36 (Cs1); 3.14−3.61 (Cs2)	2.59−3.16	2.65−3.41 (K1); 2.62−3.32 (K2)
M−O	2.86, 2.92	2.91, 2.94		3.15, 3.30 (Cs2)	3.23, 3.35 (Cs2)		2.77, 2.77	
∑bv(M−F/O)	1.04	0.87	1.11 (Rb1); 0.68 (Rb2)	1.03 (Cs1); 0.94 (Cs2)	0.94 (Cs1); 0.79 (Cs2)	0.87 (Cs1); 0.65 (Cs2)	1.01	1.16 (K1); 0.73 (K2)
∑bv(M−F)	0.67	0.54	1.11, 0.68	1.03, 0.71	0.94, 0.60	0.87, 0.65	0.65	1.16, 0.73
∑bv(M−O)	0.37 (36%)	0.33 (38%)		0.23 (24%)	0.19 (24%)		0.36 (36%)	
M···⊙	4.97−5.91	5.08−5.94	4.89−5.88 (Rb1); 5.64−5.90 (Rb2)	5.03−6.01 (Cs1); 5.16−8.14 (Cs2)	5.10−6.08 (Cs1); 5.24−8.29 (Cs2)	5.04−5.97 (Cs1); 5.15−7.98 (Cs2)	4.69−5.66	4.72−5.67 (K1); 5.45−5.65 (K2)
space group	$P2_1/c$	$P2_1/c$	$C2/c$	$P2_12_12_1$	$P2_12_12_1$	$P2_12_12_1$	$P2_1/c$	$C2/c$
FUV ($Å^3$)[d]	381.6	399.5	370.7	376.3	391.8	386.6	367.9	332.0
anion packing	distorted CsCl	distorted	hexagonal	hexagonal	hexagonal	hexagonal	distorted CsCl	hexagonal
⊙···⊙	7.17, 7.85, 9.37	7.30, 7.93, 9.49	8.51, 8.55	8.08−10.16	8.15−10.31	8.02−10.10	7.28, 9.23	8.21, 8.24
distance between anion layers	6.96	7.09	5.87	5.09 ± 0.07	5.21 ± 0.07	5.28 ± 0.05	7.09	5.67
closest M···M	4.40, 4.80[e]	4.51, 4.79[e]	5.59[f]	4.93, 5.49[g]	4.97, 5.60[g]	5.12, 5.56[g]	4.25	5.42[h]

[a] $Z^{2-} = B_{12}F_{12}^{2-}$. All results are from this work unless otherwise indicated. [b] Reference 1. [c] Reference 2. [d] FUV = formula unit volume. [e] The shorter distance is between Rb atoms in different $Rb_2(H_2O)_2$ rhombs; the longer distance is between Rb atoms in the same rhomb. [f] This is the shortest Rb1···Rb2 distance. [g] The shorter distance is between Cs1 and Cs2 atoms; the longer distance is between two Cs2 atoms. [h] This is the shortest K1···K2 distance.

DOI: 10.1021/acs.inorgchem.7b02081
Inorg. Chem. 2017, 56, 12023−12041

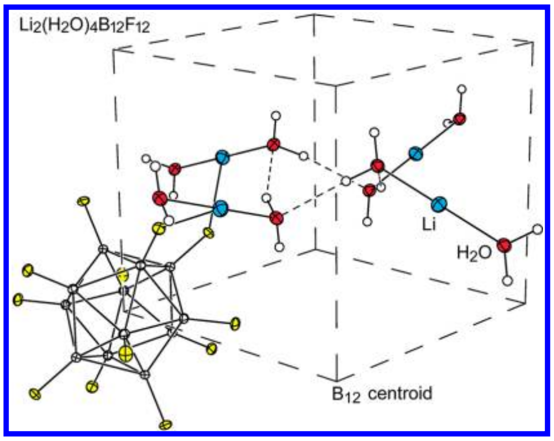

Figure 1. Structure of $Li_2(H_2O)_4(B_{12}F_{12})$ (50% probability ellipsoids except for H atoms). Only one of the eight Z^{2-} anions at the corners of the tetragonal unit cell is shown, and only one Li^+ ion is shown with its complement of four F atoms. The *trans*-LiO_2F_4 coordination sphere is shown in Figure S4. The unique Li−O distance is 1.995(1) Å. The two unique pairs of Li−F distances are 2.109(1) and 2.118(1) Å. The $(H_2O)_4$ cluster in the center of the tetragonal cell forms an O_4 skew-quadrilateral with pairs of O(H)···O distances of 2.778(1) and 2.785(1) Å and a dihedral angle of 71.7°. Another view of the skew-quadrilateral is shown in Figure S5.

centroids (⊙) form a nearly perfect tetragonal array, with ⊙···⊙ distances of 6.767, 7.287, and 7.287 Å and with ⊙···⊙···⊙ angles within 0.1° of 90°. The Li^+ ions are centered on the four 6.767 × 7.287 Å faces. Each Li^+ ion is coordinated to four F atoms, one from each of four Z^{2-} anions, with pairs of Li−F distances of 2.109(1) and 2.118(1) Å, and to two H_2O molecules arranged so that (i) the symmetry-related Li−O distances are 1.995(1) Å, (ii) the O−Li−O angle is 180°, and (iii) the H_2O molecules do not bridge two Li^+ ions. Instead, each tetragonal array of B_{12} ⊙'s contains four hydrogen-bonded H_2O molecules that form an O_4 skew-quadrilateral, with pairs of 2.778(1) and 2.785(1) Å O(H)···O distances and a dihedral angle of 71.7° [cf. crystalline H_2O-I_h, with an average O(H)···O distance of 2.76 Å]. Clusters of four H_2O molecules in solid-state structures are generally flat, nearly square arrays,[60] which is also the theoretically lowest-energy structure for an isolated $(H_2O)_4$ cluster.[61] The H atoms that are not involved in O(H)···O hydrogen bonding are weakly hydrogen-bonded to F atoms of the Z^{2-} anion [there are four O(H)···F distances that range from 2.88 to 2.97 Å]. The Li−O and Li−F bond distances and bond valences are listed in Table S19. A related structure with a cubic array of Z^{2-} anions and ⊙···⊙ distances of 7.242 Å is $K_2(HF)_3Z$ [in that case, $K_2(\mu\text{-}HF)_3^{2+}$ cations are centered in each cube of anions].[6]

The structure of $Li_2(H_2O)_4(B_{12}H_{12})$, with the same 2:4:1 stoichiometry as $Li_2(H_2O)_4Z$, has been determined by PXRD.[62] In contrast to the structure of $Li_2(H_2O)_4Z$, there are discrete $(H_2O)Li(\mu\text{-}H_2O)_2Li(H_2O)$ *dinuclear* complexes, as shown in Figure S6, in which each Li^+ ion is coordinated to two bridging H_2O ligands, one terminal H_2O ligand, and a $B_{12}H_{12}^{2-}$ anion in tridentate fashion (i.e., the Li^+ ions are six-coordinate, with three Li−O bonds and three Li−H bonds; see Table S20 for a list of bond distances and bond valences).[62] It is not clear why the cations and H_2O molecules are organized differently in the two structures, especially because the anion lattices are quite similar in size and shape. The anion parallelpiped for $Li_2(H_2O)_4Z$ shown in Figure 1, with the ⊙···⊙ distances and ⊙···⊙···⊙ angles listed in the previous paragraph, has a volume of 359 Å^3. The anion parallelpiped for $Li_2(H_2O)_4(B_{12}H_{12})$ has a volume of 340 Å^3, only 6% smaller (see Figure S6). Nevertheless, one determining factor may be the relative strengths of the Li−F and Li−H bonds. Another factor may be the absence of O(H)···O hydrogen bonding in $Li_2(H_2O)_4(B_{12}H_{12})$ and the presence of two O(H)···O hydrogen bonds per H_2O molecule in $Li_2(H_2O)_4Z$, which also exhibits additional, albeit weaker, O(H)···F hydrogen bonds.

A lithium salt hydrate with a square-pyramidal $Li(H_2O)F_4$ coordination sphere and discrete $F_2(H_2O)Li(\mu\text{-}F_2)Li(H_2O)F_2$ dimeric moieties is $Li_2Mg(H_2O)_4(ZrF_6)_2$ [Li−O = 2.016(3) Å; $\sum$bv(Li−X) = 0.97].[63] There are a number of lithium salt hydrates of other fluoroanions that, like $Li_2(H_2O)_4Z$, have $Li(H_2O)_2$ moieties and either *cis*- or *trans*-LiO_2F_4 coordination spheres. These are $Li(H_2O)(AsF_6)$,[64] $Li(H_2O)(BF_4)$,[65] $Li_2(H_2O)_2(TiF_6)$,[66] and $Li_2(H_2O)_2(SnF_6)$.[66] Table S21 lists Li−O and Li−F distances and bond valence sums [$\sum$bv(Li−X)] and Li···Li distances for these four structures and for $Li_2(H_2O)_4Z$. The most striking difference is that the H_2O/Li ratio is 2:1 in $Li_2(H_2O)_4Z$ and 1:1 in the other compounds. This can be attributed to the much larger size of Z^{2-} relative to BF_4^-, AsF_6^-, TiF_6^{2-}, and SnF_6^{2-}. For example, the Li−O and Li−F bond valence values for the *trans*-LiO_2F_4 coordination spheres in $Li_2(H_2O)_4Z$ and $Li_2(H_2O)_2(SnF_6)$ add up to 1.00 and 0.97, respectively. The 1:1 H_2O/Li stoichiometry in $Li_2(H_2O)_2(SnF_6)$ is due to the formation of $[-Li(\mu\text{-}H_2O)Li(\mu\text{-}H_2O)-]_\infty$ chains, with Li···Li distances of 3.05 Å. The Sn−F, Sn···Sn, and Li···Sn distances are 1.97, 4.73, and 3.71 Å, respectively. In contrast, the ⊙···F, ⊙···⊙, and Li···⊙ distances in $Li_2(H_2O)_4Z$ are 3.07, 6.77, and 4.97 Å, respectively. The anion lattice in $Li_2(H_2O)_4Z$ is presumably too big to allow $[-Li(\mu\text{-}H_2O)_nLi(\mu\text{-}H_2O)_n-]_\infty$ chains with Li···Li distances of only 3.1 Å to form while maintaining optimal Li−F distances. Note that the other three compounds in Table S21 also have $[-Li(\mu\text{-}H_2O)Li(\mu\text{-}H_2O)-]_\infty$ chains.

Larger metal ions such as Na^+ and Ag^+ can form such chains in a large Z^{2-} lattice: the Na···Na and Ag···Ag distances in $Na_2(H_2O)_4Z$[7] and $Ag_2(H_2O)_4Z$[45] are 3.56−3.61 and 3.54 Å, respectively, and both compounds have 2:1 H_2O/M stoichiometries and $[-M(\mu\text{-}H_2O)_2M(\mu\text{-}H_2O)_2-]_\infty$ chains. The same is true for the mixed-metal hydrate $LiK(H_2O)_4Z$, which we will discuss next.

II.C. $LiK(H_2O)_4Z$. The structure of this compound is shown in Figure 2. It consists of partially offset hexagonal layers of Z^{2-} anions with parallel $[-Li(\mu\text{-}H_2O)_2K(\mu\text{-}H_2O)_2-]_\infty$ chains between them aligned with the ADAD··· offset direction (see below). The chains consist of tetrahedral LiO_4 and compressed square-antiprismatic KO_4F_4 coordination spheres that are bridged through pairs of H_2O ligands (the KO_4F_4 coordination sphere is shown in Figure S7). Bond distances and bond valences are listed in Table S22. As mentioned in the previous paragraph, the structures of $LiK(H_2O)_4Z$, $Na_2(H_2O)_4Z$, and $Ag_2(H_2O)_4Z$ are virtually the same (except that both metal ions in the latter two compounds have MO_4F_2 coordination spheres), with parallel $[-M(\mu\text{-}H_2O)_2M(\mu\text{-}H_2O)_2-]_\infty$ chains between offset hexagonal layers of Z^{2-} anions [i.e., ADAD··· anion packing,[67] as shown in Figure S8 for $LiK(H_2O)_4Z$ and several related structures]. The formula unit volumes are 395 Å^3 (LiK), 394 Å^3 (Na), and 400 Å^3 (Ag). The M···M distances are also virtually the same, 3.516(1) Å (LiK), 3.56−3.61 Å (Na), and 3.54 Å (Ag). The $[-M(\mu\text{-}H_2O)_2M(\mu\text{-}H_2O)_2-]_\infty$ chains in $LiK(H_2O)_4Z$ and $Na_2(H_2O)_4Z$ are compared in Figure 3. Not only is the structure of $LiK(H_2O)_4Z$ significantly

DOI: 10.1021/acs.inorgchem.7b02081
Inorg. Chem. 2017, 56, 12023−12041

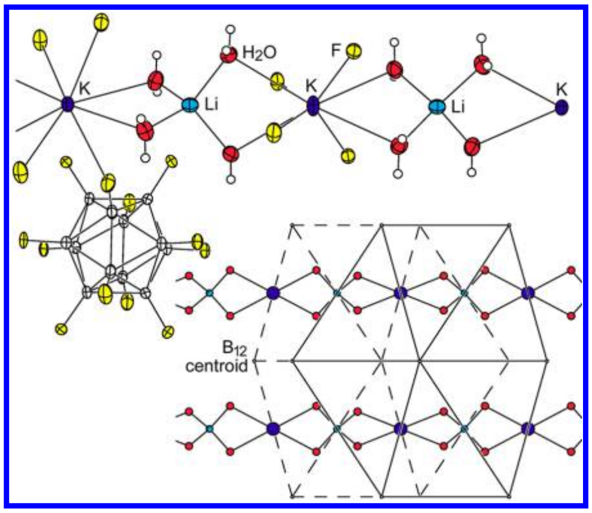

Figure 2. Structure of $LiK(H_2O)_4(B_{12}F_{12})$. The upper drawing, shown with 50% probability ellipsoids except for H atoms, shows a segment of the $[-Li(\mu\text{-}H_2O)_2K(\mu\text{-}H_2O)_2-]_\infty$ chains of tetrahedral LiO_4 and compressed square-antiprismatic KO_4F_4 coordination spheres. The lower drawing shows two parallel $[-Li(\mu\text{-}H_2O)_2K(\mu\text{-}H_2O)_2-]_\infty$ chains between two offset hexagonal layers of Z^{2-} anions (H, B, and F atoms omitted for clarity; the anions are represented by their B_{12} centroids).

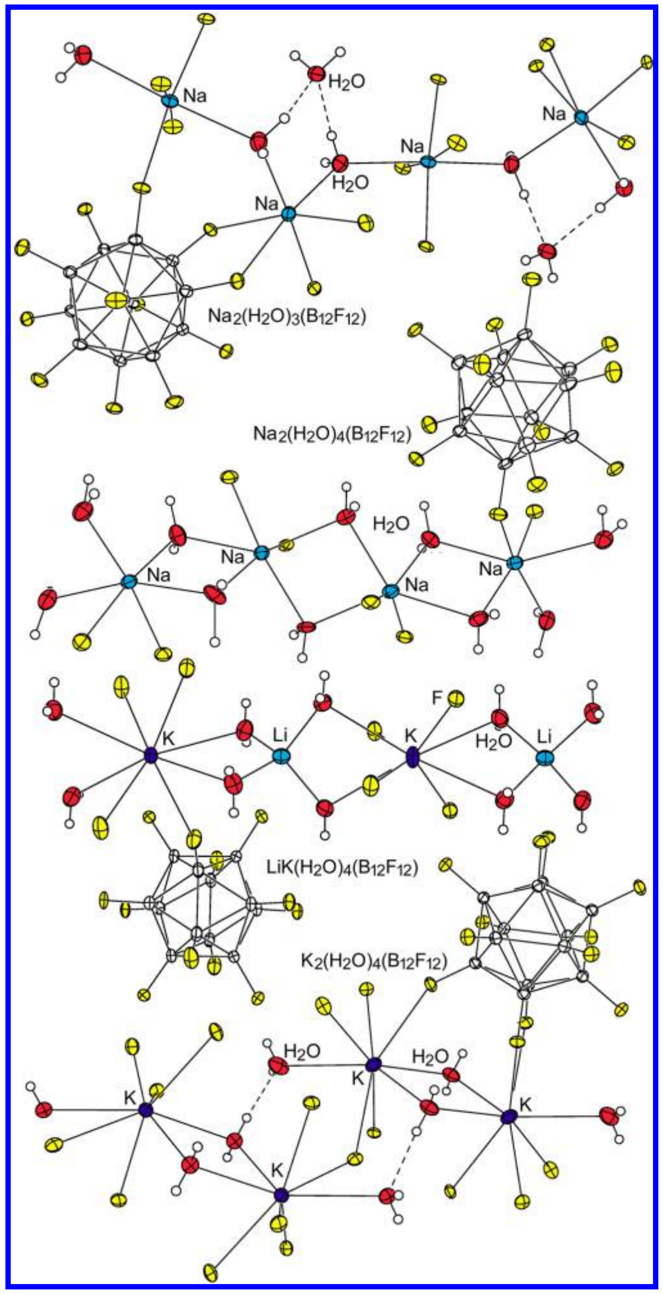

Figure 3. Comparison of 50% probability ellipsoid drawings (except for H atoms) of the structures of $Na_2(H_2O)_3Z$ (top; this work; $Z^{2-} = B_{12}F_{12}{}^{2-}$), $Na_2(H_2O)_4Z$ (second from top; ref 7), $LiK(H_2O)_4Z$ (second from bottom; this work), and $K_2(H_2O)_4Z$ (bottom; ref 1). Note the similarities between the structures of $LiK(H_2O)_4Z$ and $Na_2(H_2O)_4Z$ and the differences between the structures of $LiK(H_2O)_4Z$ and $K_2(H_2O)_4Z$.

different from the structure of $Li_2(H_2O)_4Z$, it is also significantly different from the structure of $K_2(H_2O)_4Z$, which is also shown for comparison in Figure 3. It is of interest that the sum of the four- and eight-coordinate effective ionic radii of Li^+ and K^+ is 2.10 Å (i.e., 0.59 Å + 1.51 Å = 2.10 Å) and twice the six-coordinate effective ionic radius of Na^+ is 2.04 Å (i.e., 2 × 1.02 Å = 2.04 Å), virtually the same.[68]

The four symmetry-related Li−O distances in $LiK(H_2O)_4Z$ are 1.945(3) Å, and the sum of the Li−O bond valences is 1.10. A compound with somewhat similar $Li(H_2O)_4$ coordination spheres is $Li_2(H_2O)_7(B_{12}H_{12})$, shown in Figure S10, in which one of the H_2O molecules bridges two $Li(H_2O)_3$ moieties. The Li−O distances are 1.929, 1.942 × 2, and 2.010 Å (s.u.'s were not reported),[69,70] and the sum of the Li−O bond valences is 1.07. Compounds with discrete $Li(H_2O)_4{}^+$ cations include $Li(H_2O)_4(Li(C_7H_5O_2)_2)$,[71] $Li(H_2O)_4(B(OH)_4)\cdot 2H_2O$,[72] $Li(H_2O)_4(OC(CF_3)_3)$,[73] and $Li(H_2O)_4(Al(OC(CF_3)_3)_4)$.[73] An interesting structure is $Li(H_2O)_3(AsF_6)$,[74] which is shown in Figure S10. It contains $[-Li(\mu\text{-}H_2O)_3Li(\mu\text{-}H_2O)_3-]_\infty$ chains with rare six-coordinate $Li(H_2O)_6$ coordination spheres [Li−O = 2.120 Å × 3 and 2.119 Å × 3; $\sum$bv(Li−O) = 1.03; Li···Li = 2.746 Å].

II.D. $Na_2(H_2O)_3Z$. The structure of this compound, shown in Figures 3 and 4, is unique among Z^{2-} salt hydrates characterized to date in that one of the H_2O molecules is not bonded to a metal ion; it is only hydrogen-bonded to the other H_2O molecules. The structures of $Li_2(H_2O)_4Z$ (Figure 1) and $K_2(H_2O)_4Z$[1] (Figure 3) also contain H_2O molecules that participate in O(H)···O hydrogen bonds, but in those cases, all of the H_2O molecules are bonded to the metal ions.

There are alternating *cis*- and *trans*-NaO_2F_4 coordination spheres in $Na_2(H_2O)_3Z$ that are linked to form $[-Na(\mu\text{-}H_2O)Na(\mu\text{-}H_2O)-]_\infty$ chains (the individual Na−O and Na−F bond distances and bond valences are listed in Table S23). The lattice H_2O molecule acts as a bifurcated hydrogen-bond acceptor for the pair of H_2O molecules in each *cis*-NaO_2F_4 moiety. This forms a four-atom NaO_3 array that is planar to within ±0.01 Å. It is sensible that the coordinated H_2O molecules are the hydrogen-bond donors because, by virtue of their coordination to two Na^+ ions, they should have more acidic H atoms than a lattice H_2O molecule. An interesting feature of the structure of $Na_2(H_2O)_3Z$ is that the anions are not arranged in flat close-packed layers because they are in Na_2Z,[7] $Na_2(H_2O)_4Z$,[7] $LiK(H_2O)_4Z$, K_2Z,[2] $K_2(H_2O)_4Z$,[1] and $Ag_2(H_2O)_4Z$[45] and several silver(I) solvate salts including $Ag_2(CH_3CN)_4Z$ and $Ag_2(CH_2Cl_2)_4Z$.[43] (Some of these rigorously coplanar or nearly coplanar layers of B_{12} centroids are shown in Figure S8.) Instead, the undulating snakelike $[-Na(\mu\text{-}H_2O)Na(\mu\text{-}H_2O)-]_\infty$

DOI: 10.1021/acs.inorgchem.7b02081
Inorg. Chem. 2017, 56, 12023−12041

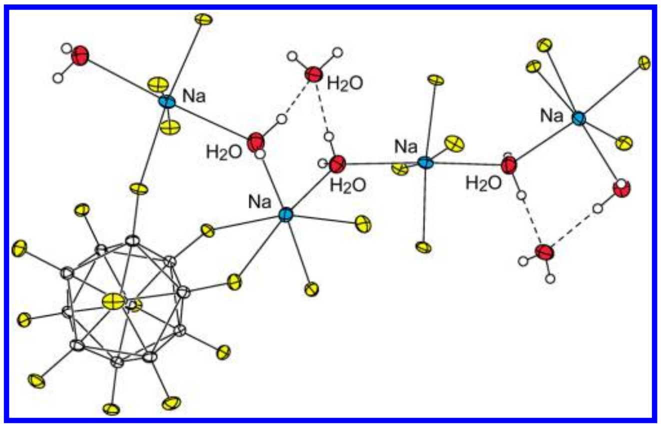

Figure 4. Part of the structure of $Na_2(H_2O)_3(B_{12}F_{12})$ (50% probability ellipsoids except for H atoms), showing the alternating *cis-* and *trans-* NaO_2F_4 coordinating units that are linked to $[-Na(\mu\text{-}H_2O)Na(\mu\text{-}H_2O)-]_\infty$ chains. The O(H)···O hydrogen-bond distances are 2.710(4) and 2.799(4) Å.

chains in $Na_2(H_2O)_3Z$ appear to cause the anions to pack in corrugated layers, as shown in Figure S11.

The $[-Na(\mu\text{-}H_2O)Na(\mu\text{-}H_2O)-]_\infty$ chains in $Na_2(H_2O)_3Z$ and the $[-Na(\mu\text{-}H_2O)_2Na(\mu\text{-}H_2O)_2-]_\infty$ chains in $Na_2(H_2O)_4Z$ are shown next to one another in Figure 3. It can be seen that three B−F bonds belonging to a Z^{2-} triangular face tightly bridge neighboring Na^+ ions along the chain in $Na_2(H_2O)_3Z$. The Z^{2-} anions do not bridge neighboring Na^+ ions along the $[-Na(\mu\text{-}H_2O)_2Na(\mu\text{-}H_2O)_2-]_\infty$ chains in $Na_2(H_2O)_4Z$.

II.E. $Rb_2(H_2O)_2Z$. The SC-XRD structures of $Rb_2(H_2O)_2Z$, shown in Figure 5, and of $K_2(H_2O)_2Z$[1] are very similar (drawings of their structures are shown side-by-side in Figure S12). Their $P2_1/c$ unit cells have similar volumes (763 vs 736 Å^3, respectively), their average ⊙···⊙ distances are 7.39 and 7.28 Å^3, respectively, and the Rb···Rb and K···K distances within the $M_2(\mu\text{-}H_2O)_2$ rhombs are 4.797(1) and 4.2529(3) Å, respectively. The bond valence sums $\sum$bv(M−O) and $\sum$bv(M−F) are 0.37 and 0.67, respectively, for $Rb_2(H_2O)_2Z$ and 0.35 and 0.65, respectively, for $K_2(H_2O)_2Z$. Two differences are (i) RbO_2F_8 versus KO_2F_6 coordination spheres and (ii) the shortest Rb···Rb distance is 4.400(1) Å, shorter by ca. 0.4 Å than the distance between Rb^+ ions in the same $Rb_2(\mu\text{-}H_2O)_2$ rhomb. In contrast, the shortest distance between K^+ ions that are not in the same $K_2(\mu\text{-}H_2O)_2$ rhomb is 5.0750(3) Å, more than 0.8 Å longer that the distance between K^+ ions in the same $K_2(\mu\text{-}H_2O)_2$ rhomb. A comparison of the SC-XRD structure of $Rb_2(H_2O)_2Z$ with other rubidium salt hydrates will be discussed in section III.E.

To validate the DFT code that we used to calculate the structures of hydrated and anhydrous Rb^+ and Cs^+ salts of Z^{2-}, we first compared the SC-XRD and DFT-optimized structures of K_2Z and $K_2(H_2O)_2Z$. The results are shown in Tables S2−S4. The pairs of structures are virtually the same except that the DFT distances are greater, as is commonly found when using a Vanderbilt-type ultrasoft potential with PBE exchange correlation (i.e., the interaction potentials are typically underestimated, resulting in larger lattice constants than those experimentally observed).[75] The expansion of the K_2Z formula unit volume upon hydration to $K_2(H_2O)_2Z$ is 10.8% (18.0 Å^3 per H_2O) for the 120/110 K SC-XRD structures[1,2] and 11.9% (20.8 Å^3 per H_2O) for the DFT structures. Bond distances and bond valences for the SC-XRD and DFT structures of K_2Z and $K_2(H_2O)_2Z$ are listed in Tables S5−S8. The bond valences for the two $K-OH_2$ bonds are 36 and 37% of the total bond

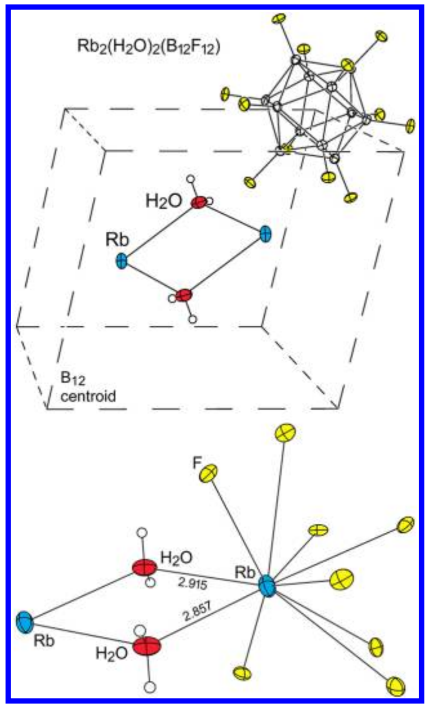

Figure 5. Structure of $Rb_2(H_2O)_2(B_{12}F_{12})$ (50% probability ellipsoids except for H atoms). The irregular RbO_2F_8 coordination sphere is shown for only one of the symmetry-related Rb^+ ions. The Rb−O distances (Å) are shown. The Rb−F distances range from 2.909(1) to 3.237(1) Å. The Rb···Rb distance in the $Rb_2(\mu\text{-}H_2O)_2$ rhomb is 4.797(1) Å.

valences for the SC-XRD and DFT structures of $K_2(H_2O)_2Z$, respectively.

Unit cell parameters, fractional coordinates, bond distances, and bond valences for the DFT-optimized structures of Rb_2Z and $Rb_2(H_2O)_2Z$, and bond distances and bond valences for the SC-XRD structure of $Rb_2(H_2O)_2Z$, are listed in Tables S9−S13. Important distances and formula unit volumes are listed in Table 3. The DFT-optimized structure of Rb_2Z and the SC-XRD structure of K_2Z[2] are isomorphous ($C2/c$; Z = 4). They have a $B8_2$-Ni_2In-like structure,[76] with half of the metal ions in O_h holes and half of the metal ions in D_{3h} holes in the expanded close-packed layers of Z^{2-} anions. The DFT and SC-XRD structures of $Rb_2(H_2O)_2Z$ are also very similar (both have $P2_1/c$ lattices with Z = 2). These two structures are compared in Figure S13 and Table 3. At the DFT level of theory, the Rb_2Z formula unit volume expansion upon hydration to $Rb_2(H_2O)_2Z$ is 7.77% (14.4 Å^3 per H_2O). Experimental unit cell parameters for Rb_2Z and $Rb_2(H_2O)_2Z$ were determined by PXRD at room temperature (see the Experimental Methods section). The expansion of the Rb_2Z formula unit volume upon hydration to $Rb_2(H_2O)_2Z$ was found to be 9.14% (16.4 Å^3 per H_2O) at 24 °C. There is no doubt that the Rb_2Z lattice must expand in order to absorb H_2O. In addition, because the PXRD sample of $Rb_2(H_2O)_2Z$ was prepared from the PXRD sample of Rb_2Z by hydration in the presence of water vapor [hereinafter $H_2O(g)$], there is also no doubt that the transformation $Rb_2Z + 2H_2O \rightarrow Rb_2(H_2O)_2Z$ is a crystal-to-crystal transformation, similar to what was previously shown for the $K_2Z + 2H_2O \rightarrow K_2(H_2O)_2Z$ transformation.[1]

II.F. DFT Structures of Cs_2Z and $Cs_2(H_2O)Z$. Interestingly, the DFT computations for Cs_2Z strongly suggest that its structure is not isomorphous with the $C2/c$ DFT structure of

DOI: 10.1021/acs.inorgchem.7b02081
Inorg. Chem. 2017, 56, 12023−12041

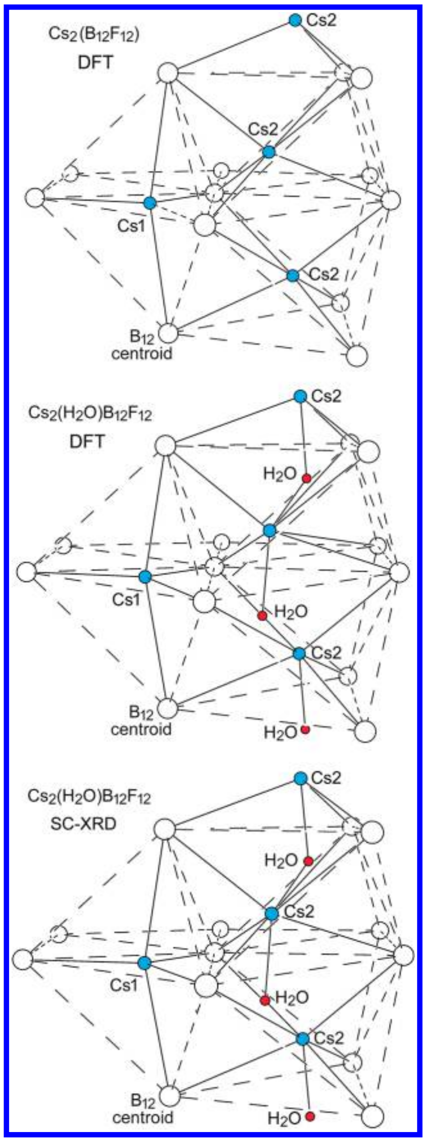

Figure 6. DFT structures of Cs_2Z (top) and $Cs_2(H_2O)Z$ (middle) and the SC-XRD structure of $Cs_2(H_2O)Z$ (bottom; ref 2). The large spheres are B_{12} centroids.

Rb_2Z and the DFT and SC-XRD structures of K_2Z. A reasonable alternative structure with the same $P2_12_12_1$ symmetry as that experimentally observed for $Cs_2(H_2O)Z$ was found to be considerably lower in energy than the $C2/c$ structure. In fact, the DFT structures of Cs_2Z and $Cs_2(H_2O)Z$ and the SC-XRD structure of $Cs_2(H_2O)Z$ all have nearly the same $P2_12_12_1$ structure with respect to the positions of the anions and cations, as shown in Figure 6. They all have a distorted variant of the $B8_2$-Ni_2In-like structures of K_2Z and Rb_2Z, in which the pseudo-close-packed layers of B_{12} centroids (⊙) are not rigorously coplanar (the centroids deviate from planarity by ±0.07 Å). The results listed in Tables 3 and S16−S18 show that the Cs−F, Cs···⊙, and ⊙···⊙ distances and the distances between the ⊙ planes are quite similar for Cs_2Z and $Cs_2(H_2O)Z$. For example, the perpendicular distances between the least-squares planes of anion centroids are 5.28, 5.21, and 5.09 Å for DFT Cs_2Z, DFT $Cs_2(H_2O)Z$, and SC-XRD $Cs_2(H_2O)Z$, respectively. Nevertheless, there is a small, but finite, 5.2 $Å^3$ expansion of the DFT Cs_2Z lattice to accommodate each H_2O molecule upon hydration to DFT $Cs_2(H_2O)Z$.

III. Dehydration/Rehydration of Z^{2-} Salt Hydrates.

III.A. Kinetic versus Thermodynamic Factors. In 2010, we reported that microcrystalline K_2Z was hydrated to $K_2(H_2O)_2Z$ in a matter of minutes at 25 °C in a continuous purge of He containing 21 Torr of $H_2O(g)$ and dehydrated at 25 °C in a continuous purge of dry He in less than 1 h.[1] In addition, we determined that (i) the equilibrium vapor pressure of water $[P(H_2O)]$ for the $K_2(H_2O)_2Z \rightleftharpoons K_2Z + 2H_2O(g)$ equilibrium at 25 °C is 6.1(3) Torr and (ii) the enthalpy change (ΔH) for the forward reaction is 55.5 kJ (mol of $H_2O)^{-1}$.[1] The ΔH values for the partial or complete dehydration of eight other potassium salt hydrates range from 56.0 to 70.2 kJ (mol of $H_2O)^{-1}$ [av. 60.7 kJ (mol of $H_2O)^{-1}$].[77] Figure S14 is a plot of $\Delta H°$ versus $P(H_2O)$ for these eight compounds and for $K_2(H_2O)_2Z$ (the individual values[77] are listed in Table S24). It is clear that the $K_2(H_2O)_2Z \rightleftharpoons K_2Z + 2H_2O(g)$ equilibrium is not unusual thermodynamically. It is the kinetics of $K_2(H_2O)_2Z$ dehydration and K_2Z rehydration that are unusual. The K_2Z lattice rapidly and reversibly expands by ca. 11% in a matter of minutes *at room temperature* to accommodate the two H_2O molecules, a change equal to 18.0 $Å^3$ per H_2O at the 110 or 120 K temperatures of the SC-XRD structures and probably equal to ca. 20 $Å^3$ per H_2O at room temperature. For comparison, the average effective volume of a H_2O molecule in a wide variety of alkali-metal and alkaline-earth salt hydrates is 24.5 $Å^3$ (the 34 individual values ranged from 20.4 to 28.9 $Å^3$; the anions were halides, hydroxides, and various oxoanions).[78−80]

We can put into perspective the rapidity with which the $K_2Z \leftrightarrow K_2(H_2O)_2Z$ transformations occur by a comparison with two other potassium hydrates of 2− fluoroanions. The dihydrate $K_2(H_2O)_2(SnMe_2F_4)$, which has virtually the same $K_2(\mu\text{-}H_2O)_2^{2+}$ core as $K_2(H_2O)_2Z$ (see Table S25), undergoes dehydration at a measurable rate only above 75 °C.[81] The monohydrate $K_2(H_2O)(AlF_5)$, in which the H_2O molecule bridges two K^+ ions with K−O distances considerably *longer* than those in $K_2(H_2O)_2Z$ (see Table S26), undergoes dehydration at a measurable rate only above 60 °C and was not completely dehydrated, at a heating rate of 3 °C min^{-1}, until the temperature reached 140 °C.[82] Furthermore, the anhydrous salt $K_2(AlF_5)$ required several *days* to rehydrate back to $K_2(H_2O)(AlF_5)$ at 25 °C. For these reasons, our focus in the remainder of this paper will be on the unusual rates, not the extents, of dehydration and rehydration of structurally characterized $M_2(H_2O)_nZ$ compounds that are not microporous. We use the term *latent porosity* to describe the behavior of a nonporous crystalline material that undergoes unusually rapid and reversible volume changes to accommodate the absorption/desorption of reactive gases at 25 ± 5 °C.[1]

III.B. Dehydration of $Li_2(H_2O)_4Z$ and $LiK(H_2O)_4Z$. TGA traces for these two compounds are shown in Figure 7. In contrast to the rapid partial or complete dehydration at 25 °C of $LiK(H_2O)_4Z$, $Na_2(H_2O)_nZ$ (n = 3, 4), $K_2(H_2O)_nZ$ (n = 2, 4),[1] $Rb_2(H_2O)_2Z$, and $Cs_2(H_2O)Z$ (see below), the lithium salt hydrate $Li_2(H_2O)_4Z$ did not lose any significant amount of coordinated H_2O molecules in dry N_2 at 25 °C over nearly 3 h. It began to lose H_2O above 40 °C and, with a heating rate of 1.5 °C min^{-1}, was completely dehydrated at ca. 140 °C. The anhydrous salt Li_2Z was rehydrated when it was exposed to N_2 containing 13 Torr of $H_2O(g)$, as shown in Figure S15.

For comparison, it was reported that the compound $Li_2(H_2O)_7(B_{12}H_{12})$ began to lose coordinated H_2O molecules as soon as it was heated above 25 °C, as shown in Figure S16.[69]

DOI: 10.1021/acs.inorgchem.7b02081
Inorg. Chem. 2017, 56, 12023−12041

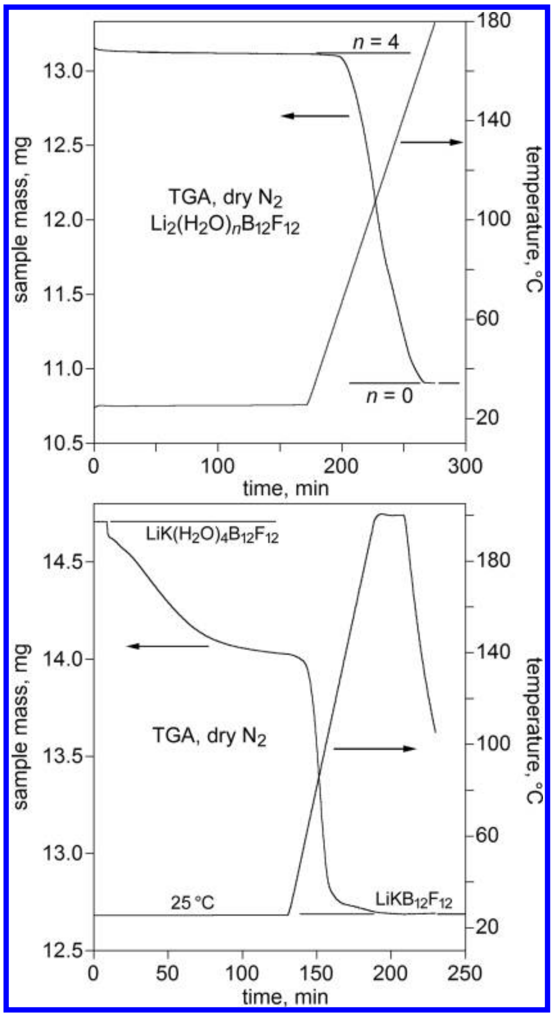

Figure 7. TGA plots showing the complete dehydration of $Li_2(H_2O)_4(B_{12}F_{12})$ to $Li_2(B_{12}F_{12})$ (top) and of $LiK(H_2O)_4(B_{12}F_{12})$ to $LiK(B_{12}F_{12})$ (bottom). In the latter experiment, the sample had lost a small amount of H_2O at 25 °C after it was weighed but before the TGA data collection began. ^1H, $^{11}B\{^{19}F\}$, and $^{19}F\{^{11}B\}$ NMR spectra of the anhydrous compounds $Li_2(B_{12}F_{12})$ and $LiK(B_{12}F_{12})$, taken after heating, showed that only a negligible amount of H_2O was present (possibly due to adventitious H_2O from the glovebox atmosphere) and that no observable degradation of the Z^{2-} cluster had occurred.

At 68 °C, the composition was $Li_2(H_2O)_4(B_{12}H_{12})$, which did not lose additional H_2O molecules until it was heated above 105 °C. The anhydrous salt $Li_2(B_{12}H_{12})$ was formed at ca. 160 °C[69] and was stable until 250 °C, after which it decomposed with the evolution of H_2.[83] (Note that Li_2Z is stable until heated above 400 °C.[41]) The compound $Li(H_2O)_4(B(OH)_4)\cdot 2H_2O$[72] lost the four H_2O molecules coordinated to the Li^+ ion between 60 and 120 °C.[84] The compound $Li_4(H_2O)_3(B_8O_{13}(OH)_2)$, in which each of the three H_2O molecules is coordinated in a terminal fashion to three of the four Li^+ ions, loses H_2O in stages beginning at 100 °C.[85] The compound $Li_2Mg(H_2O)_4(ZrF_6)_2$, with square-pyramidal $Li(H_2O)F_4$ coordination spheres, lost all four of the coordinated H_2O molecules in one stage between 105 and 200 °C.[63] As far as we are aware, there is no salt hydrate that rapidly evolves, in an inert gas at 25 °C, one or more H_2O molecules that are coordinated *only* to Li^+.

In contrast to the behavior of $Li_2(H_2O)_4Z$, the mixed-metal salt hydrate $LiK(H_2O)_4Z$ lost 1.0−1.2 equiv of H_2O in ca. 60 min at 25 °C. Mass loss slowed considerably after that until the sample was heated above 40 °C. At a constant heating rate of 3 °C min^{-1}, the sample lost all of the remaining H_2O molecules and was transformed, after ca. 60 min, into anhydrous LiKZ at 200 °C. Given the structure of $LiK(H_2O)_4Z$, there is no doubt that the loss of the first H_2O molecule involves breaking a Li−OH bond as well as a K−OH_2 bond. Rehydration of anhydrous LiKZ was not studied because of the possibility of phase separation into, for example, Li_2Z and K_2Z. This possibility will be studied by PXRD in our future work.

III.C. Rapid Room-Temperature Partial Dehydration/Rehydration of $Na_2(H_2O)_4Z$. We recently published the structure and dehydration behavior of $Na_2(H_2O)_4Z$.[7] The dehydration TGA is shown in Figure 8. The tetrahydrate phase rapidly lost

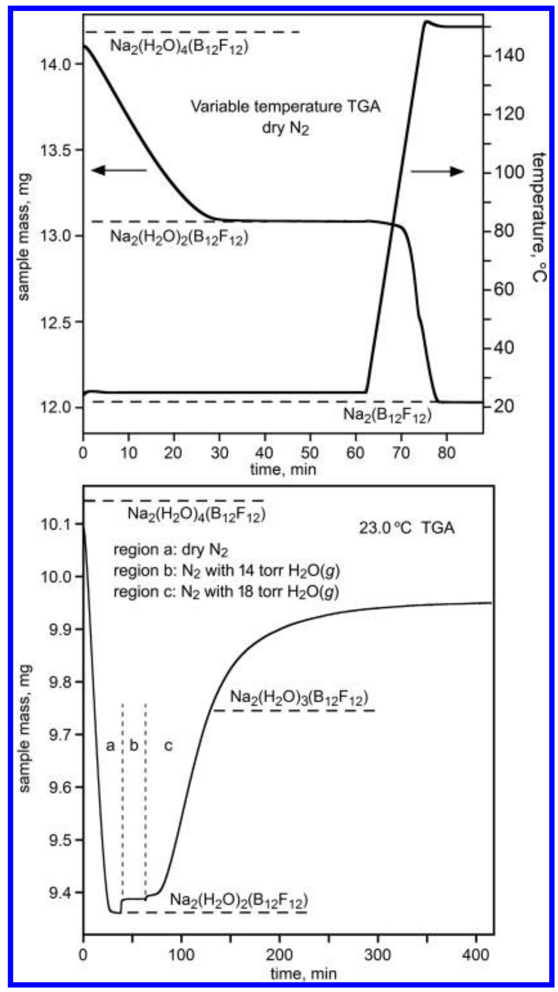

Figure 8. TGA experiments with $Na_2(H_2O)_4Z$ ($Z^{2-} = B_{12}F_{12}^{2-}$). The upper experiment shows the rapid dehydration of $Na_2(H_2O)_4Z$ to $Na_2(H_2O)_2Z$ in dry N_2 in ca. 30 min at 25 °C, the resistance of $Na_2(H_2O)_2Z$ to further dehydration at 25 °C, and its complete dehydration at temperatures above 70 °C. The lower experiment, performed at a constant temperature of 23 °C, shows that $Na_2(H_2O)_2Z$ rapidly absorbs only a small amount of H_2O under 14 Torr of $H_2O(g)$, absorbs 1.0 equiv of H_2O in ca. 70 min under 18 Torr of H_2O, and absorbs additional H_2O very slowly after the composition has exceeded $Na_2(H_2O)_3Z$.

2.0 equiv of H_2O in a flowing dry N_2 atmosphere in ca. 30 min at 25 °C, with no indication of the intermediacy of a trihydrate phase. Repeated attempts to crystallize and obtain the structure of $Na_2(H_2O)_2Z$ under a variety of conditions only resulted in the crystallization of $Na_2(H_2O)_3Z$ or $Na_2(H_2O)_4Z$. The dihydrate

DOI: 10.1021/acs.inorgchem.7b02081
Inorg. Chem. 2017, 56, 12023−12041

phase, $Na_2(H_2O)_2Z$, did not lose any measurable amount of H_2O at 25 °C, even after several hours. Heating the sample to 150 °C did result in the formation of anhydrous Na_2Z. Direct comparisons of the similar structures and similar TGA dehydration behavior of $Na(H_2O)_4Z$ and $LiK(H_2O)_4Z$ are shown in Figure S17.

The rehydration of $Na_2(H_2O)_2Z$ at 23 °C in N_2-containing $H_2O(g)$ is also shown in Figure 8. Bulk rehydration did not occur when $P(H_2O)$ was 14 Torr but did occur rapidly at 18 Torr. With $P(H_2O)$ = 14 Torr, a small mass increase (ca. 0.05 equiv of H_2O) commensurate with, presumably, surface rehydration, occurred in less than 1 min, but thereafter the mass did not increase even after an extended period of time (not shown). When $P(H_2O)$ was changed from 14 to 18 Torr, the mass increased somewhat beyond the composition "$Na_2(H_2O)_3Z$" in only 70 min (from 60 to 130 min in the particular isothermal experiment shown in the bottom half of Figure 8) but then tapered off significantly. The transformation from "$Na_2(H_2O)_3Z$" to $Na_2(H_2O)_4Z$ took an additional 24 h (not shown). The use of quotation marks is intended to indicate a particular $Na_2(H_2O)_nZ$ composition with $n \approx 3$, not necessarily a specific trihydrate phase. Nevertheless, the shape of the $Na_2(H_2O)_2Z$ rehydration curve indicates that the transformation of $Na_2(H_2O)_2Z$ to $Na_2(H_2O)_4Z$ under 18 Torr of $H_2O(g)$ almost certainly involves the intermediacy of at least one $Na_2(H_2O)_nZ$ phase where $3 \leq n < 4$. Even if we assume that only one intermediate phase is present, it is not known if n is 3.0 or some fractional number between 3 and 4. In fact, the TGA plot suggests that $n > 3$. However, even if n = 3.0, the structure of the putative intermediate phase would not necessarily be the same as the $P2_12_12_1$ polymorph of $Na_2(H_2O)_3Z$ determined in this work by SC-XRD and shown in Figures 3 and 4. In ongoing work, we plan to address these questions by collecting time-resolved PXRD data during $Na_2(H_2O)_2Z$ rehydration.

Regardless of the structure of the $Na_2(H_2O)_nZ$ intermediate phase, we determined that it is dehydrated in dry N_2 even faster than it is formed from $Na_2(H_2O)_2Z$ under 18 Torr of $H_2O(g)$. Three complete cycles carried out at 23 °C are shown in Figure 9. The carrier gas was changed from N_2/18 Torr of $H_2O(g)$ to dry N_2 when the sample composition just exceeded "$Na_2(H_2O)_3Z$" and from dry N_2 to N_2/18 Torr of $H_2O(g)$

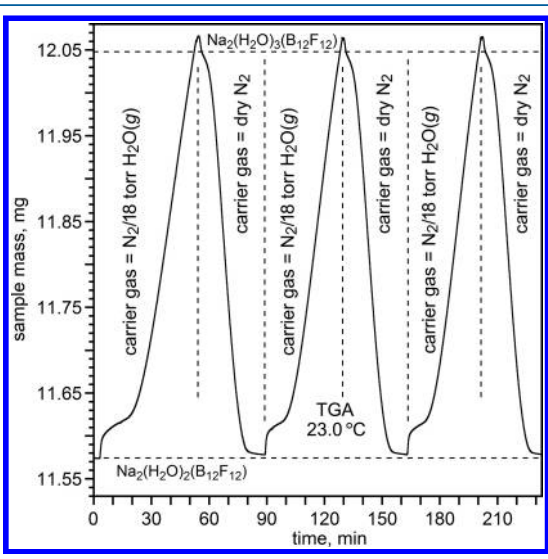

Figure 9. Three complete $Na_2(H_2O)_2 \leftrightarrow$ "$Na_2(H_2O)_3Z$" hydration/dehydration cycles at 23 °C.

when the sample mass had returned to within 1% $Na_2(H_2O)_2Z$. The first cycle was complete in ca. 90 min, and the subsequent cycles were complete in ca. 70 min. It can therefore be said that $Na_2(H_2O)_2Z$ exhibits latent porosity.

Each 18 Torr of $H_2O(g)$ rehydration in Figure 9 began with a very rapid mass increase of ca. 0.05 equiv of H_2O in ca. 1 min, which was followed by a much slower mass increase during the next 10 min, which was followed by the bulk of the hydration from $Na_2(H_2O)_2Z$ to "$Na_2(H_2O)_3Z$" over the next 30−35 min. As in our previous latent porosity study,[1] we define a pair of kinetic figures of merit that are useful for comparing the results of different hydration/dehydration cycles: the maximum rate of the bulk of the hydration of a particular sample, rh_{max}, and the maximum rate of the bulk of the dehydration of the same sample at the same temperature, rd_{max}. They are the absolute values of the maximum slopes of the hydration and dehydration TGA segments and therefore are easy to determine. They can be expressed in mg min^{-1} or %(total mass change) min^{-1}. One of their uses is to determine the reproducibility of the rates of hydration and dehydration for consecutive cycles with a given sample. For example, for the three $Na_2(H_2O)_2Z \leftrightarrow$ "$Na_2(H_2O)_3Z$" cycles shown in Figure 9, rh_{max} was 3.4, 3.8, and 4.0%(change) min^{-1} and rd_{max} for all three cycles was 6.6%(change) min^{-1}. However, rh_{max}, rd_{max}, and the ratio rh_{max}/rd_{max}, which is dimensionless, are not intended to be used in any mathematical equation related to a mechanistic model or an equilibrium constant.

As discussed in more detail below, we are not in a position to propose and test possible mechanisms of hydration and dehydration in this study. Nevertheless, anticipating a more detailed kinetic/mechanistic study in future work, we point out that the shape of the TGA hydration curves following the (presumed) rapid surface hydration resembles nucleation and growth models that have been proposed for many solid-state reactions, phase transformations, and crystallizations,[86,87] including salt hydrate dehydrations and rehydrations.[88,89] As we shall see, the shapes of the $Na_2(H_2O)_2Z$ hydration TGA curves also resemble the shapes of the hydration curves for isothermal TGA experiments with microcrystalline samples of K_2Z, Rb_2Z, and Cs_2Z, which will be discussed next.

III.D. Latent Porosity in K_2Z, Rb_2Z, and Cs_2Z. The 10−15 mg samples of these compounds that were used in TGA hydration/dehydration cycle experiments were finely ground for 10+ min in an agate mortar and pestle. Scanning electron micrographs of samples of K_2Z and Cs_2Z are shown in Figure S18. A majority of the individual particles are blocks or plates for which the largest dimension is ca. 1 μm or less. There are also some larger particles with dimensions up to ca. 5 μm, as well as conglomerates of many small particles that may or may not be welded together.

As in our previous study of K_2Z hydration/dehydration at 25 °C,[1] we will not attempt to fit the TGA data to one or more specific solid-state reaction kinetic functions at this time because many important variables such as the particle size uniformity, particle-surface-area-to-volume ratio, crystallinity, surface roughness, etc., were not controlled in the experiments reported here. There are a large number of "mechanisms" (i.e., kinetic functions) by which hydrates as simple as monohydrates have been proposed to undergo dehydration, and one such kinetic function, or even a small number of possible functions, can rarely be assigned unambiguously because different functions usually fit the (almost always *non*isothermal) mass change versus time data equally well.[89−93]

DOI: 10.1021/acs.inorgchem.7b02081
Inorg. Chem. 2017, 56, 12023−12041

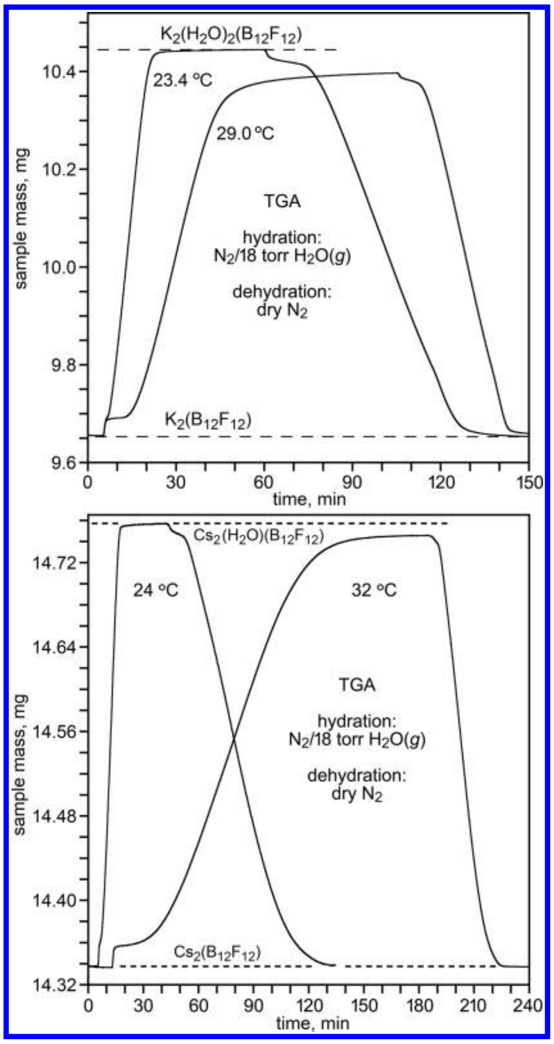

Figure 10. TGA plots of hydration/dehydration experiments at two temperatures with K_2Z (top) and Cs_2Z (bottom). The carrier gas was changed ca. 1 min before the increase or decrease in mass (i.e., not at 0 min for the hydration segments). The same sample was used at both temperatures in each of the experiments.

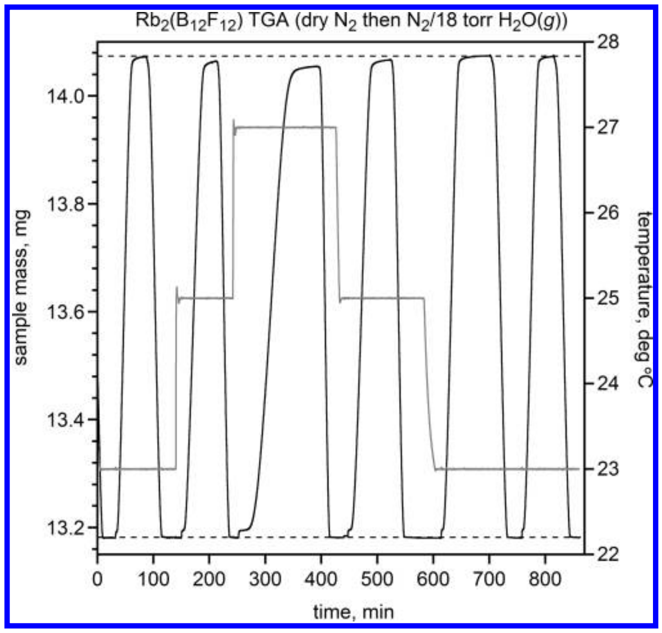

Figure 11. TGA hydration/dehydration cycles for a single sample of Rb_2Z at 23.0, 25.0, and 27.0 °C. The carrier gas for the hydration segments was N_2 containing 18 Torr of $H_2O(g)$. The carrier gas for the dehydration segments was dry N_2. The carrier gas was changed ca. 0.5 min before the increase or decrease in mass in each segment was observed. The horizontal dotted lines correspond to the masses of Rb_2Z and $Rb_2(H_2O)_2Z$. The superimposed step-function plot shows the temperature changes from 23 to 25 to 27 to 25 to 23 °C before and after each of the six hydration/dehydration cycles.

Galwey[94] and others[86,95] have pointed out the erroneous way that the term reaction *mechanism* has been equated with *a particular kinetic function* in many thermal analyses of solid-state reactions, as opposed to the more chemically relevant, non-mathematical, and widely accepted definition of a reaction mechanism as the "complete sequence of all simple [chemical] steps through which reactants are converted into products".[94] These caveats notwithstanding, the TGA results presented and discussed here can be *tentatively* described in terms of the generic chemical processes of (i) rapid surface hydration or dehydration of a particle of Z^{2-} salt, (ii) relatively slow formation of one or more hydrated or dehydrated phases on the surface of the particle, and (iii) rapid growth of the new phase(s) throughout the particle (i.e., bulk hydration or dehydration). Note that these descriptions are only intended to facilitate the discussion and to serve as tentative hypotheses to be tested in future work on the hydration/dehydration behavior of these and other Z^{2-} salt hydrates.

Complete isothermal hydration/dehydration cycles at two temperatures are shown in Figure 10 for the same sample of K_2Z (23.4 and 29.0 °C) and for the same sample of Cs_2Z (24.0 and 32.0 °C). Multiple cycles at 23.0, 25.0, and 27.0 °C for Rb_2Z are shown in Figure 11. Several features are noteworthy. First, the fully hydrated masses at room temperature (23−24 °C) correspond, to better than ±0.7%, to the stoichiometries of the structurally characterized hydrates $K_2(H_2O)_2Z$,[1] $Rb_2(H_2O)_2Z$ (this work), and $Cs_2(H_2O)Z$[2] (i.e., typically to better than ±5 μg starting with a ca. 13 mg sample of anhydrous salt). For example, the ratio of masses for the first and last hydrations of Rb_2Z to $Rb_2(H_2O)_2Z$ at 23 °C shown in Figure 11 are 0.9366 (13.181 mg/14.072 mg) and 0.9365 (13.181 mg/14.074 mg), respectively, whereas the ratio of the two molar masses is 0.9362 [(528.648 g mol^{-1})/(564.679 g mol^{-1})]. Second, each hydration and dehydration segment begins with a rapid (ca. 1−2 min) increase or decrease in mass, respectively, that corresponds to, at most, a few percent of the total mass change, which, as discussed above, is tentatively attributed to the formation of a hydrated or dehydrated surface layer or layers. This is followed by a sigmoid-shaped region that constitutes the bulk of the mass change. Third, the previously defined rh_{max} and rd_{max} values occur when the sample is ca. 50% hydrated or dehydrated, respectively. For example, for the 24.0 °C $Cs_2Z \leftrightarrow Cs_2(H_2O)Z$ TGA shown in Figure 10, rh_{max} was 0.0451 mg min^{-1} (10.8% min^{-1}) and rd_{max} was 0.00791 mg min^{-1} (1.9% min^{-1}). Fourth, for a given sample, the hydration and dehydration TGA segments for multiple cycles at the same temperature are virtually superimposable, even when cycles at other temperatures are run between them. This is shown for two consecutive 23.4 °C $K_2Z \leftrightarrow K_2(H_2O)_2Z$ cycles in Figure S19. There are also three 23 °C and two 25 °C $Rb_2Z \leftrightarrow Rb(H_2O)_2Z$ cycles in Figure 10 that can be compared in this way. Fifth, the fully hydrated mass of each sample, but not the fully dehydrated mass, decreased slightly as the temperature increased. Sixth, rh_{max} and rd_{max} are strongly temperature-dependent. This is readily

DOI: 10.1021/acs.inorgchem.7b02081
Inorg. Chem. 2017, 56, 12023−12041

apparent in Figure 10. For both sets of TGA plots in this figure, $rh_{max} > rd_{max}$ at the lower temperature (23.4 or 24.0 °C) and $rh_{max} < rd_{max}$ at the higher temperature (29.0 or 32.0 °C). The individual values are listed in Tables S27–S29, and plots of the ratio rh_{max}/rd_{max} versus temperature are shown for all three salt hydrate pairs in Figure 12. Room-temperature figures of merit for

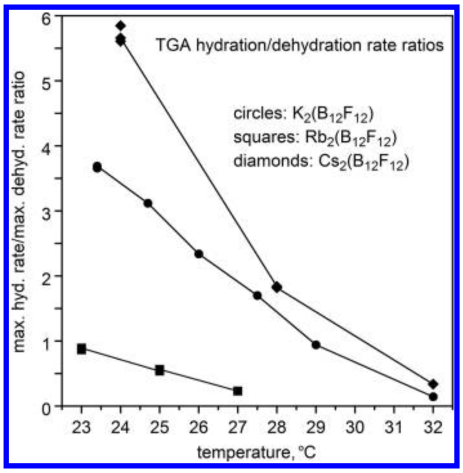

Figure 12. Temperature dependence of the ratio rh_{max}/rd_{max} for hydration/dehydration TGA experiments with microcrystalline samples of K_2Z, Rb_2Z, and Cs_2Z. The carrier gas for the hydration segments was N_2-containing 18 Torr of $H_2O(g)$. The carrier gas for the dehydration segments was dry N_2. The individual rh_{max} and rd_{max} values are listed in Tables S27–S29, respectively. For each compound, a single sample was used at all of the different temperatures.

samples of all three compounds are listed in Table 4. Plots of rh_{max} versus temperature are shown in the Table of Contents graphic.

Close inspection of Figure 11 reveals that the differences between the "fully hydrated" mass of $Rb_2(H_2O)_nZ$ ($n \leq 2$) and the constant, 13.181 mg, fully dehydrated mass of Rb_2Z were 0.893(1) mg at 23 °C [i.e., 99.3% of the theoretical value of 0.898 mg assuming the exact stoichiometry $Rb_2(H_2O)_2Z$], 0.884(1) mg at 25 °C, and 0.874 mg at 27 °C. This means that Rb_2Z absorbed only 99% as much H_2O at 25 °C than at 23 °C and only 98% as much at 27 °C than at 23 °C. This behavior was also observed for hydration/dehydration cycles of a 9.655 mg sample of K_2Z, as shown in Figure S20. The mass increase at 23.4 °C was 0.792 mg, which is 99.4% of the theoretical value of 0.797 mg assuming the exact stoichiometry $K_2(H_2O)_2Z$. Between 23.4 and 32.0 °C, the "fully hydrated" mass decreased monotonically to 0.772 mg, 96.9% of the theoretical value. These observations are consistent with, but by no means prove, the presence of H_2O vacancies in the maximally hydrated compounds, potentially even at ca. 23 °C, which presumably increase in number with increasing temperature. This behavior will be studied in more detail in an ongoing investigation.

The possible presence of H_2O vacancies may be one of the keys to understanding how it is possible for $D_2O(g)$ to replace the H_2O molecules in the "fully hydrated" compound nearly as quickly as $H_2O(g)$ is absorbed by the anhydrous salt in the first place. This was reported for $K_2(H_2O)_2Z$ in ref 1 (see Figure S2). We have now determined that $Rb_2(H_2O)_2Z$ also undergoes complete H_2O/D_2O exchange rapidly when exposed to 16 Torr of $D_2O(g)$ at room temperature, as shown in Figure 13. The solid-state hydration reaction $Rb_2Z(s)$ + $2H_2O(g)$ → $Rb(H_2O)_2Z(s)$ and the solid-state exchange

Table 4. Hydration and Dehydration TGA Figures of Merit[a]

temperature, °C	24.7	25.0	24.0
dehydrated formula	K_2Z	Rb_2Z	Cs_2Z
dehydrated mass, mg	9.655	13.181	14.338
hydrated formula	$K_2(H_2O)_2Z$	$Rb_2(H_2O)_2Z$	$Cs_2(H_2O)Z$
hydrated mass, mg	10.441	14.073(1)	14.756
mass change, mg	0.786	0.892(1)	0.418
rh_{max}, mg min^{-1}	0.0589	0.0310[b]	0.0451
rh_{max}, %(change) min^{-1}	7.4	3.5[b]	10.8
rd_{max}, mg min^{-1}	0.0189	0.0576[b]	0.00791
rd_{max}, %(change) min^{-1}	2.4	6.5[b]	1.9
rh_{max}/rd_{max} ratio	3.1	0.54[b,c]	5.7
98% hydration time, min	18	40	16
98% dehydration time, min	61	25	76
dehydrated/hydrated mass ratio	0.9247	0.9366(1)	0.9717
formula mass ratio	0.9237	0.9362	0.9719

[a] $Z^{2-} = B_{12}F_{12}^{2-}$. A single sample was used to determine all of these parameters for each compound. The carrier gas for the hydration segments was N_2 containing 18 Torr of $H_2O(g)$. The carrier gas for the dehydration segments was dry N_2. Molar masses (g mol^{-1}): K_2Z, 435.909; $K_2(H_2O)_2Z$, 471.940; Rb_2Z, 528.648; $Rb_2(H_2O)_2Z$, 564.679; Cs_2Z, 623.524; $Cs_2(H_2O)Z$, 641.539. [b] These values are for the first cycle. [c] See Figure 12 for the consistency of this ratio over three hydration/dehydration cycles at 23.0 °C.

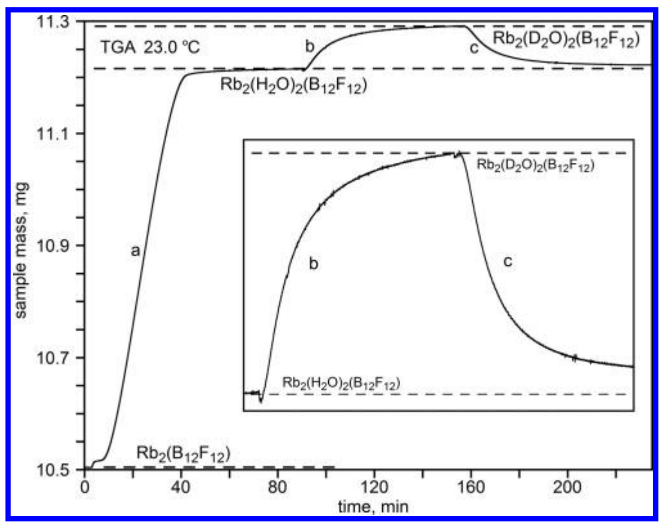

Figure 13. TGA plot showing the hydration of Rb_2Z to $Rb_2(H_2O)_2Z$ in 60 min in the presence of 18 Torr of $H_2O(g)$ (segment a) and the subsequent solid-state (i.e., gas–solid) H_2O/D_2O exchange reactions $Rb_2(H_2O)_2Z + 2D_2O(g) \rightarrow Rb(D_2O)_2Z + 2H_2O(g)$ in 64 min in the presence of 16 Torr of $D_2O(g)$ (segment b) and $Rb_2(D_2O)_2Z$ + $2H_2O(g) \rightarrow Rb(H_2O)_2Z + 2D_2O(g)$ in ca. 80–90 min in the presence of 18 Torr of $H_2O(g)$ (segment c). The inset is an expansion of the H_2O/D_2O exchange reactions. The temperature of the sample was held at 23.0 °C throughout the entire experiment.

reaction $Rb_2(H_2O)_2Z(s)$ + $2D_2O(g)$ → $Rb(D_2O)_2Z(s)$ + $2H_2O(g)$ both occurred in ca. 1 h at room temperature. However, unlike the hydration reaction, the H_2O/D_2O exchange reaction does not involve a solid-state phase change. This means that the Rb-coordinated H_2O molecules continuously diffuse through the fully hydrated $Rb_2(H_2O)_2Z$ lattice at room temperature (i) at least as fast as $D_2O(g)$ molecules replace the H_2O molecules and (ii) at least as fast as the bulk of the growth of the $Rb_2(H_2O)_2Z(s)$ phase from the $Rb_2Z(s)$ phase occurred during the hydration reaction. [Note that a control experiment

DOI: 10.1021/acs.inorgchem.7b02081
Inorg. Chem. 2017, 56, 12023–12041

with $K_2(H_2{}^{18}O)_2Z$ and H_2O, reported in ref 1, ruled out the possibility that the observed rapid H_2O/D_2O exchange involved proton transfer instead of intact isotopically labeled water molecules rapidly diffusing through the lattice and replacing H_2O molecules.]

III.E. Comparisons with Literature K^+, Rb^+, and Cs^+ Salt Hydrates. As discussed in ref 1, the latent porosity behavior of K_2Z is highly unusual, if not unprecedented, with respect to the behavior of other potassium salt hydrates, which require higher temperatures and/or significantly longer times to lose their coordinated H_2O molecules. Comparisons with $K_2(H_2O)_2(SnMe_2F_2)$ and $K_2(H_2O)AlF_5$ were discussed in section III.A. Comparisons with $K(H_2O)MnPO_4$, $K(H_2O)Zn_{2.5}V_2O_7(OH)_2$, and a microporous synthetic potassium gallosilicate natrolite were discussed in ref 1. Another example from the literature is $K_4(H_2O)_4(P_2S_6)$,[96] with KO_2S_6 and KO_4S_4 coordination spheres, which began to evolve H_2O only at 50 °C and, with a heating rate of 5 °C min^{-1}, did not form anhydrous $K_4(P_2S_6)$[97] until the temperature was 68 °C, as shown in Figure S21. Although neither TGA nor DSC/DTA results have been reported for the sructurally characterized compound $K_2(H_2O)_{0.5}(Pt(NO_3)_4)$, its crystals are "stable for a couple of weeks when kept in a desiccator protected from light".[98] Finally, although its structure is not known, the compound $K_2(H_2O)_2(Fe(CN)_5(NO))$ did not lose H_2O until it was heated above 25 °C, displaying two DTA peaks associated with H_2O loss at 64 and 96 °C, as shown in Figure S22.[99]

The rapid *room-temperature* latent porosity behavior we now report for Rb_2Z and Cs_2Z also appears to have no recognized parallel in the literature. Table S30 is a list of bond distances and bond valences for $Rb_2(H_2O)_2Z$ and seven other structurally characterized rubidium salt hydrates for which TGA results are available. The compound $Rb_4(H_2O)_6(P_2S_6)$ apparently did not lose H_2O readily because it "was recrystallized from water at 60 °C placing the solution in a vacuum desiccator".[96] The compound $Rb_2(H_2O)_{1.5}(B_4O_5(OH)_4))$, with $Rb(H_2O)O_9$ and $Rb(H_2O)_2O_6$ coordination spheres, two types of $Rb(\mu\text{-}H_2O)Rb$ bridges, and rather long $Rb-OH_2$ distances of 3.123(4)–3.392(4) Å, did not lose any significant amount of H_2O until heated above 100 °C.[100] The H_2O molecules in $Rb_2(H_2O)_2(HPO_4)$ bridge four Rb^+ ions, which have either $Rb(H_2O)_4O_4$ or $Rb(H_2O)_4O_8$ coordination spheres, with $Rb-OH_2$ distances of 2.943(2)–3.178(2) Å.[101] This compound did not lose H_2O under vacuum at room temperature, even after several days.[101] Anhydrous $Rb_2(Fe(CN)_5NO)$ was formed, and a DTA peak was observed at 67 °C, when the monohydrate $Rb_2(H_2O)(Fe(CN)_5NO)$ was heated at 5 °C min^{-1} (the H_2O molecule bridges the two types of Rb^+ ions, which have $RbON_6$ and $RbON_7$ coordination spheres).[102] The hydrated rubidium/molybdenum bronze $Rb(H_2O)(MoO_3)_{4.55}$ did not lose H_2O under vacuum for 48 h at room temperature and lost one H_2O molecule per Rb^+ ion at 70 °C.[103] The compound $Rb(H_2O)(HMTA)I$ (HMTA = hexamethylenetetramine) has an $Rb_2(H_2O)_2$ diamond-shaped moiety similar to the one in $Rb_2(H_2O)_2Z$, with Rb–O distances of 2.898(4) and 2.963(4) Å, an O–Rb–O angle of 92.7(1)°, and an Rb–O–Rb angle of 87.3(1)°.[104] This compound lost the coordinated H_2O molecule only when heated above 58 °C.[104] The compound $Rb(H_2O)_2(LH_4)$ has two $Rb(H_2O)O_8$ coordination spheres with terminal $Rb-OH_2$ bond distances of 2.837(2) and 3.056(2) Å (LH_4 is the monoanion of 4-amino-1-hydroxybutylidine-1,1-bisphosphonic acid; one of the H_2O molecules in the formula unit is a lattice H_2O molecule and is not bonded to the Rb^+ cations).[105] This compound did not lose any H_2O until heated above 133 °C, as shown in Figure S23.[105] The compound $Rb_8(H_2O)_{14}(Ta_6O_{19})$ did not begin to lose H_2O until ca. 70 °C, as shown in Figure S24. The composition stabilized at $Rb_8(H_2O)_4(Ta_6O_{19})$ at 110 °C and only began to lose H_2O again at ca. 175 °C, becoming anhydrous $Rb_8(Ta_6O_{19})$ at ca. 260 °C.[106] Finally, the compound $Rb_6(H_2O)_4(Mo_7O_{24})$, with both doubly and triply bridging H_2O molecules, did not begin to lose H_2O until heated to 100 °C and, at a heating rate of 10 °C min^{-1}, did not become completely dehydrated until ca. 180 °C, as shown in Figure S25.[107]

There are fewer structurally characterized cesium salt hydrates for which TGA results are available. Figure S24 shows the TGA plot for $Cs_8(H_2O)_{14}(Ta_6O_{19})$, which did not begin to lose H_2O until it was heated above 60 °C.[106] The same was true for $Cs_6(H_2O)_{19}(U_{24}O_{75})$[108] and $Cs_2(H_2O)_2(HPO_4)$,[109] and the latter compound did not form anhydrous $Cs_2(HPO_4)$ until it was heated to 180 °C.[109] The compound $Cs_2(H_2O)_2(Si_2O_5)$ began to lose H_2O at 80 °C and formed anhydrous $Cs_2(Si_2O_5)$ at ca. 200 °C.[110] The compound $Cs_2(H_2O)_3(B_4O_5(OH)_4)$ began to lose H_2O only when it was heated above 100 °C.[111] The only literature cesium hydrate that comes closest to exhibiting what may be latent porosity is $Cs_2(H_2O)(Fe(CN)_5(NO))$.[112] This compound apparently did not lose H_2O when held at 25 °C but began to lose H_2O soon after it was heated and had become anhydrous $Cs_2(Fe(CN)_5(NO))$ by the time the temperature reached 43 °C, as shown in Figure S26 (the heating rate was not reported).[112] The X-ray structure of the anhydrous compound, but not of the hydrate, has been reported.[113]

III.F. A Closer Look at Latent Porosity. We have shown that K_2Z, Rb_2Z, and Cs_2Z exhibit what we describe as latent porosity. The compounds $K_2(B_{12}H_{12})$, $Rb_2(B_{12}H_{12})$, and $Cs_2(B_{12}H_{12})$ do not exhibit latent porosity with respect to absorbing $H_2O(g)$: these anhydrous compounds are crystallized from aqueous solution.[70,114] Two modifications of $Rb_2(H_2O)_2(B_{12}(OH)_{12}))$ have been reported, both with RbO_{10} coordination spheres.[115,116] One contains $[-Rb(\mu\text{-}H_2O)Rb(\mu\text{-}H_2O)-]_\infty$ chains;[115] the other has a terminal H_2O ligand on each Rb^+ ion.[116] However, no dehydration results have yet been reported for either modification. Interestingly, the salt $Cs_2(B_{12}Br_{12})$ appears to be microporous as far as hydration is concerned. The three compounds $Cs_2(B_{12}Br_{12})$, $Cs_2(H_2O)(B_{12}Br_{12})$, and $Cs_2(H_2O)_2(B_{12}Br_{12})$ all crystallize in the $R\overline{3}$ space group and have nearly identical unit cell parameters and hence nearly identical formula unit volumes (they differ by less than 1%; see Table S31 for details).[70,117] Therefore, unlike $Cs_2(B_{12}F_{12})$, the $Cs_2(B_{12}Br_{12})$ lattice does not expand and contract upon hydration and dehydration, respectively. However, no observations about the rates of hydration of $Cs_2(B_{12}Br_{12})$ in the presence of $H_2O(g)$ or the dehydration of either hydrate in the absence of $H_2O(g)$ have been reported. This should be investigated in the future.

At the risk of confounding kinetics with thermodynamics, let us consider the following questions. To what can we attribute the latent porosity of K_2Z, Rb_2Z, and Cs_2Z, behavior that may be all but unprecedented as far as metal salts that are not microporous are concerned? What allows H_2O molecules to break their $M-OH_2$ bonds and O–H⋯F hydrogen bonds so quickly *as well as diffuse through the respective hydrate lattice so quickly*? It is not because $M-OH_2$ bonds are especially weak. As mentioned above, the enthalpy of dissociation of H_2O from $K_2(H_2O)_2Z$ is 55.5 kJ (mol of $H_2O)^{-1}$,[1] and this is not an unusually low value. In fact, the superweak nature of the Z^{2-}

DOI: 10.1021/acs.inorgchem.7b02081
Inorg. Chem. 2017, 56, 12023–12041

anion might be expected to make metal ions only slowly give up their coordinated H_2O ligands. The metal-ion coordination spheres in $K_2(H_2O)_2Z$ and $Rb_2(H_2O)_2Z$ are KO_2F_6 and RbO_2F_8, and 25% of the eight K−X bonds and 20% of the 10 Rb−X bonds (i.e., the two K−OH_2 and Rb−OH_2 bonds) account for 35% and 36% of the total bond valence of the metal ions, respectively (X = O, F). By this criterion, the average Rb−OH_2 bond is about twice as strong as the average Rb−F bond in $Rb_2(H_2O)_2Z$.

It may be significant that $Li_2(H_2O)_4Z$ does not lose any amount of H_2O at temperatures lower than 40−50 °C but that both $LiK(H_2O)_4Z$ and $Na_2(H_2O)_4Z$ lose one or two H_2O molecules in 120 or 30 min, respectively, at room temperature. The four H_2O molecules in $Li_2(H_2O)_4Z$ are trapped in the center of a cage of Li^+ and Z^{2-} ions and are strongly hydrogen-bonded into an $(H_2O)_4$ cluster. In addition, unlike the H_2O molecules in $LiK(H_2O)_4Z$ and $Na_2(H_2O)_4Z$, the H_2O molecules in $Li_2(H_2O)_4Z$ do not bridge two metal ions, precluding a relatively low activation energy path for diffusion of H_2O through the lattice. There are no infinite chains of metal ions and bridging H_2O molecules in $K_2(H_2O)_2Z$ and $Rb_2(H_2O)_2Z$ (the K···K and Rb···Rb distances in the $K_2(\mu\text{-}H_2O)_2$ and $Rb_2(\mu\text{-}H_2O)_2$ rhombs are 4.253 and 4.797 Å, respectively). Nevertheless, the H_2O/D_2O exchange reactions show that H_2O diffusion through the hydrated salt lattice, which must involve the transfer of H_2O molecules between rhombs, is rapid. This may be because the next-shortest K···K distance, which is between two rhombs, is 5.075 Å, only 20% longer than 4.253 Å, and the shortest Rb···Rb distance between rhombs is 4.400 Å, 8% *shorter* than the distance within the rhombs. Note that there are $[-Cs(\mu\text{-}H_2O)Cs(\mu\text{-}H_2O)-]_\infty$ infinite chains running through the lattice in $Cs_2(H_2O)Z$.[2] Finally, none of the H_2O molecules in $LiK(H_2O)_4Z$, $Na_2(H_2O)_4Z$, $K_2(H_2O)_2Z$, $Rb_2(H_2O)_2Z$, and $Cs_2(H_2O)Z$ is hydrogen-bonded to another H_2O molecule in the lattice, The H_2O ligands are only weakly hydrogen-bonded to B−F bonds of the anions. It remains to be seen what effect the O−H···O hydrogen-bonded lattice H_2O molecule in $Na_2(H_2O)_3Z$ has on the rate of dehydration or further hydration at room temperature.

Table 5 lists structural results and information about the rates of dehydration for selected K^+, Rb^+, and Cs^+ salt hydrates. Neither the M^+/H_2O ratio, the M^+/anion ratio, the lattice volume per M^+ ion, the lattice volume change per H_2O molecule that is desorbed from the lattice, nor the percent of the total metal-ion bond valence due to the M−OH_2 bonds can explain the rapid and reversible room-temperature dehydration of $K_2(H_2O)_2Z$, $Rb_2(H_2O)_2Z$, and $Cs_2(H_2O)Z$ relative to the other salt hydrates. The only significant difference is the lack of O−H···O hydrogen bonding in the three Z^{2-} compounds and its presence in the structures of most of the other compounds [the exceptions are $K_2(H_2O)_{0.5}(Pt(NO_3)_4)$, in which the H_2O molecule bridges four K^+ ions, and both $K_2(H_2O)(Fe(CN)_5(NO))$ and $Rb_2(H_2O)(Fe(CN)_5(NO))$, in which each H_2O ligand bridges two K^+ or Rb^+ ions and participates in two O−H···N hydrogen bonds].

The latent porosity we have observed may be related to the SC-XRD and/or DFT structures of K_2Z, Rb_2Z, Cs_2Z, $K_2(H_2O)_2Z$, $Rb_2(H_2O)_2Z$, and $Cs_2(H_2O)Z$, three of which are

Table 5. Comparison of Structural and Dehydration Results for Selected K^+, Rb^+, and Cs^+ Salt Hydrates

compd	M^+/H_2O	M^+/anion	$V(M^+)$, Å^3	$V(H_2O)$, Å^3	% bv from M−OH_2	rapid dehydration at 23−24 °C
$K_2(H_2O)_4(B_{12}F_{12})$[a]	1:2	2:1	212.1	23.1[b]	50, 56	yes
$K_2(H_2O)_2(B_{12}F_{12})$[a]	1:1	2:1	184.0	18.0[b]	35	yes
$K_2(H_2O)_{0.5}(Pt(NO_3)_4)$[c]	4:1	2:1	145.0		11	no[c]
$K_2(H_2O)(Fe(CN)_5(NO))$[d]	2:1	2:1	135.7		23, 28	no[e]
$K_4(H_2O)_4(P_2S_6)$[f]	1:1	4:1	101.5	18.5[g]	33, 51	no[f]
$Rb_2(H_2O)_2(B_{12}F_{12})$[h]	1:1	2:1	190.8	16.4[h]	36	yes[h]
$Rb_4(H_2O)_6(P_2S_6)$[i]	2:3	4:1	121.0	19.9[g]	24, 36	no[i]
$Rb_6(H_2O)_4(Mo_7O_{24})$[j]	3:2	6:1	118.5		13−31	no[j]
$Rb_8(H_2O)_{14}(Ta_6O_{19})$[k]	4:7	8:1	116.2		45−62	no[k]
$Rb_8(H_2O)_4(Ta_6O_{19})$[k]	2:1	8:1	78.5		17−39	no[k]
$Rb_2(H_2O)(LH_4)\cdot H_2O$[l]	2:1	2:1	306.7		8.3, 22	no[m]
$Rb_2(H_2O)(Fe(CN)_5(NO))$[n]	2:1	2:1	135.7	16.6[o]	17	no[n]
$Cs_2(H_2O)(B_{12}F_{12})$[p]	2:1	2:1	188.2	5.2[q]	25[q]	yes[q]
$Cs_4(H_2O)_6(P_2S_6)$[i]	2:3	4:1	131.4		22, 35	no[i]
$Cs_8(H_2O)_{14}(Ta_6O_{19})$[k]	4:7	8:1	116.2	21.5[r]	45−57	no[s]
$Cs_2(H_2O)(Fe(CN)_5(NO))$	2:1	2:1	166.4[t]			no[u]

[a]Reference 1; the M−OH_2 bonds have the second and third highest bond valence (bv). [b]The structure of anhydrous $K_2(B_{12}F_{12})$ was published in ref 2. [c]Reference 118; crystals were "stable for a couple of weeks when kept in a desiccator protected from light". [d]Reference 119; the structural results in this table are for the monohydrate. [e]Reference 99; TGA/DTA plots indicate that dehydration of the *dihydrate* takes place in two stages, with DTA peaks at 64 and 96 °C. [f]Reference 96; see Figure S21; dehydration occurred slowly between 50 and 68 °C upon heating at 5 °C min^{-1}. [g]The structures of anhydrous $K_2(P_2S_6)$ and $Rb_2(P_2S_6)$ were published in ref 106. [h]This work; the highest bv is for an M−OH_2 bond. [i]Reference 96; the compound "was recrystallized from water at 60 °C placing the solution in a vacuum desiccator". [j]Reference 107; no mass loss until heating above 100 °C. [k]Reference 106; the loss of 10 H_2O molecules from $Rb_8(H_2O)_{14}(Ta_6O_{19})$ occurred between 68 and 100 °C; the loss of the remaining four H_2O molecules occurred only above 175 °C (see Figure S24). [l]Reference 105. [m]Junk, P. C. Personal communication, 2016 (see Figure S23). [n]Reference 102; dehydration produced "a DTA peak located at 67 °C". [o]The structure of anhydrous $Rb_2(Fe(CN)_5(NO))$ was published in ref 120. [p]Reference 2; the highest bv is for an M−OH_2 bond. [q]This work; the sum of the Cs−OH_2 bond valences was also 25% in the DFT-optimized structure. [r]The structure of anhydrous $Cs_8(Ta_6O_{19})$ was published in ref 106. [s]Reference 106; the loss of 10 H_2O molecules from $Cs_8(H_2O)_{14}(Ta_6O_{19})$ occurred between 65 and 150 °C; the loss of the remaining four H_2O molecules occurred between 150 and 200 °C (see Figure S24). [t]From the structure of anhydrous $Cs_2(Fe(CN)_5(NO))$, published in ref 113 (the structure of the hydrate is not known). [u]Reference 112; heating a sample resulted in a DTA peak at 43 °C (see Figure S26).

DOI: 10.1021/acs.inorgchem.7b02081
Inorg. Chem. 2017, 56, 12023−12041

reported in this work for the first time. They are all based on a "slipped" variation of a hexagonal close-packed lattice of Z^{2-} anions, and only relatively minor adjustments of anions within the close-packed layers and minor adjustments of the M···M distances are required for hydration to occur (see Table 3; the changes in the M···M distances upon hydration are 1.2 Å for K^+, 0.8 Å for Rb^+, and <0.1 Å for Cs^+). This can be readily seen in Figure 6 for the hydration of Cs_2Z to $Cs_2(H_2O)Z$. This can also be seen for the hydration of K_2Z, or Rb_2Z (not shown), to its respective hydrate in Figure 14. Although the K_2Z lattice

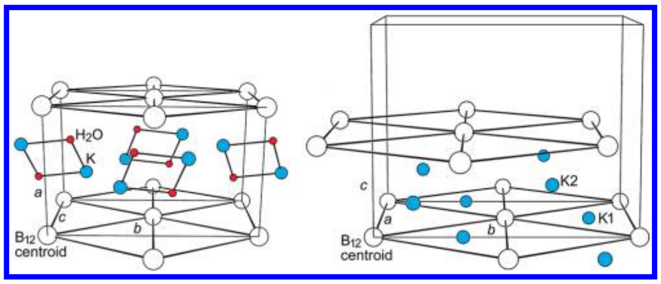

Figure 14. Drawings of the SC-XRD structures of $K_2(H_2O)_2Z$ (left; ref 1) and K_2Z (right; ref 2). The drawings are to scale in the plane of the page, but the greater depth in the drawing of $K_2(H_2O)_2Z$ (c = 9.23 Å) than in the drawing of K_2Z (a = 8.21 Å) is not readily apparent. From the standpoint of the B_{12} centroid (⊙) in the center of each hexagonal array of anions, the hydration results in two 8.21 Å ⊙···⊙ distances in K_2Z lengthening to 9.23 Å in $K_2(H_2O)_2Z$ and four 8.24 Å ⊙···⊙ distances in K_2Z shortening to 7.28 Å in $K_2(H_2O)_2Z$.

expands by ca. 11% upon hydration, most of this change is in the spacing between the close-packed layers of anions. For the hydration of K_2Z to occur, two 8.21 Å ⊙···⊙ distances within the anion layers lengthen to 9.23 Å and four 8.24 Å ⊙···⊙ distances shorten to 7.28 Å. According to the DFT structures, for the hydration of Rb_2Z to occur, two 8.51 Å ⊙···⊙ distances within the anion layers lengthen to 9.49 Å and four 8.55 Å ⊙···⊙ distances shorten to either 7.30 or 7.93 Å.

Solid-state ^{11}B and ^{1}H NMR studies have shown that the $B_{12}H_{12}^{2-}$ anions in $M_2(B_{12}H_{12})$ salts (M = Na, K, Rb, Cs) and the $B_{12}Cl_{12}^{2-}$ anions in $Cs_2(B_{12}Cl_{12})$ undergo rapid rotational reorientations about their fixed lattice positions and fixed lattice orientations even at room temperature.[121,122] [At higher temperatures, rotational disorder (i.e., multiple orientations around fixed lattice positions), frequently accompanied by phase transitions, has been observed by NMR and quasi-elastic neutron scattering measurements.[122−125]] Such reorientations of the Z^{2-} anions in K_2Z, Rb_2Z, Cs_2Z, and their hydrates, even if they are not completely isotropic, could conceivably facilitate the ≤1.2 Å cation rearrangements between close-packed anion layers and the concomitant ca. 1 Å anion rearrangements within the close-packed layers that accompany hydration and dehydration. Furthermore, the "turnstyle" motion of the anions about fixed positions in the hydrates could facilitate the migration of H_2O and D_2O molecules through the fully hydrated lattices by "handing off" sets of O−H···F(B) hydrogen bonds between neighboring anions.

III.G. (Apparent) Negative Activation Energies. The results in Table S27 show that rh_{max} for K_2Z *decreased* by more than a factor of 10 as the temperature *increased* from 23.4 to 32.0 °C. For Rb_2Z, rh_{max} decreased by 2.6 times when the temperature was increased by just 4 °C, from 23.0 to 27.0 °C (see Table S28). For Cs_2Z, rh_{max} decreased by nearly 8 times as the temperature increased from 24.0 to 32.0 °C (see Table S29). This so-called "negative kinetic temperature effect", sometimes said to indicate "a negative activation energy", is uncommon in condensed-phase chemical kinetics in general[126−129] and is only rarely encountered in solid-state reactions.[130−133] In solution, an apparent negative activation energy can be due to an equilibrium prior to the rate-determining step that shifts to the left with increasing temperature. In the case of the hydration of M_2Z salts, it is possible that a surface hydration equilibrium controls the overall rate of hydration. This interesting phenomenon, and its possible causes, will be studied in an ongoing investigation.

III.H. Thermal Stability of Anhydrous M_2Z Salts (Z^{2-} = $B_{12}F_{12}^{2-}$). Previously reported TGA experiments and before-and-after ^{19}F NMR spectra for Li_2Z, K_2Z, and Cs_2Z demonstrated that they are stable with respect to cluster degradation until they are heated above 400, 500, and 600 °C, respectively,[41] and that Na_2Z is stable up to at least 327 °C.[7] In this work, we have determined that the anhydrous salt Rb_2Z is stable up to ca. 460 °C, as shown in Figure S27. We did not examine the thermal stability of LiKZ because of the ambiguity regarding possible phase separation into Li_2Z and K_2Z upon dehydration of $LiK(H_2O)_4Z$.

For comparison, anhydrous $LiPF_6$ decomposes at 133 °C,[134] $LiPF_6$ exposed to air [i.e., $H_2O(g)$] at 91−105 °C[135,136], $LiBF_4$ at 162−243 °C[135,136] (the wide range may also be a function of whether the salt is rigorously anhydrous), $LiN(SO_2F)_2$ at 200 °C,[137] $Li(1\text{-}MeCB_{11}F_{11})$ at 300 °C,[41] $LiN(SO_2CF_3)_2$ at 340 °C,[135] $LiCF_3SO_3$ at 425 °C,[135] and $K(B(3,5\text{-}C_6H_3(CF_3)_2)_4)$ at 350 °C.[138] We are not aware of a report about the thermal stability of a Rb^+ salt of a weakly coordinating anion.

4. CONCLUSIONS

A complete set of structures, SC-XRD, PXRD, and/or DFT, of anhydrous and hydrated Na^+, K^+, Rb^+, and Cs^+ salts of the Z^{2-} anion, including three new structures reported in this work, is now available. Latent porosity behavior, previously observed for $K_2Z \leftrightarrow K_2(H_2O)_2Z$ hydration/dehydration cycles at room temperature,[1] has now been observed for $Na_2Z(H_2O)_2 \leftrightarrow Na_2(H_2O)_3Z$, $Rb_2Z \leftrightarrow Rb_2(H_2O)_2Z$, and $Cs_2Z \leftrightarrow Cs_2(H_2O)Z$ hydration/dehydration cycles at 23−32 °C. This behavior stands in sharp contrast to virtually all other structurally characterized K^+, Rb^+, and Cs^+ salt hydrates for which dehydration information is available, which require higher temperatures and/or significantly longer times to lose the coordinated H_2O molecules. The latent porosity of K_2Z, Rb_2Z, and Cs_2Z may be related to four structural factors: (i) only minor adjustments of the anion positions in the close-packed layers of anions, and only minor changes of the M···M distances, are required for hydration to occur; (ii) hydrogen bonding between H_2O and the F atoms of Z^{2-} is weaker, which may facilitate more rapid migration through a lattice, than hydrogen bonding between H_2O and anions such as HPO_4^{2-}, $B_4O_5(OH)_4^{2-}$, $Pt(NO_3)_4^{2-}$, $Fe(CN)_5(NO)^{2-}$, $Mo_7O_{24}^{6-}$, $Ta_6O_{19}^{8-}$, or even $P_2S_6^{4-}$; (iii) the nearly spherical Z^{2-} anion may undergo rotational reorientations more rapidly and/or more isotropically than the aforementioned anions, and this could facilitate the cation and anion rearrangements that accompany hydration and dehydration in the Z^{2-} salts; (iv) rotational reorientations, if they occur at room temperature, could also facilitate the migration of H_2O molecules through the hydrated salt lattices by trading sets of O−H···F(B) hydrogen bonds between neighboring anions as they rotate (i.e., handing off H_2O molecules from anion to anion with little loss of hydrogen bonding). In addition, because $Rb_2(H_2O)_2Z$ undergoes

DOI: 10.1021/acs.inorgchem.7b02081
Inorg. Chem. 2017, 56, 12023−12041

complete H_2O/D_2O exchange in 60 min at 23 °C when exposed to 16 Torr of $D_2O(g)$, we conclude that the Rb-coordinated H_2O molecules continuously diffuse through the $Rb_2(H_2O)_2Z$ lattice at room temperature (i) at least as fast as $D_2O(g)$ molecules replace the H_2O molecules and (ii) at least as fast as the growth of the $Rb_2(H_2O)_2Z(s)$ phase from the $Rb_2Z(s)$ phase during the hydration reaction (which took only ca. 30 min). Finally, the rate of hydration of K_2Z, Rb_2Z, and Cs_2Z decreased significantly with increasing temperature. This uncommon phenomenon in solid-state kinetics may be related to a diminished amount of surface hydration as the temperature is increased. All of these hypotheses, and the search for latent porosity in other salt hydrate pairs, are being studied in an ongoing investigation.

■ ASSOCIATED CONTENT

Supporting Information

The Supporting Information is available free of charge on the ACS Publications website at DOI: 10.1021/acs.inorgchem.7b02081.

Additional figures and tables and complete refs 47 and75 (PDF)

Accession Codes

CCDC 1567680−1567683 contain the supplementary crystallographic data for this paper. These data can be obtained free of charge via www.ccdc.cam.ac.uk/data_request/cif, or by emailing data_request@ccdc.cam.ac.uk, or by contacting The Cambridge Crystallographic Data Centre, 12 Union Road, Cambridge CB2 1EZ, UK; fax: +44 1223 336033.

■ AUTHOR INFORMATION

Corresponding Authors

*E-mail: peryshkov@sc.edu (D.V.P.).
*E-mail: bukovsky1@llnl.gov (E.V.B.).
*E-mail: steven.strauss@colostate.edu (S.H.S.).

ORCID

Dmitry V. Peryshkov: 0000-0002-5653-9502
Hui Wu: 0000-0003-0296-5204
Wei Zhou: 0000-0002-5461-3617
Matic Lozinšek: 0000-0002-1864-4248
Steven H. Strauss: 0000-0001-7636-2671

Present Address

E.V.B.: Lawrence Livermore National Laboratory, Livermore, CA.

Notes

The authors declare no competing financial interest.

■ ACKNOWLEDGMENTS

We thank Dr. Brian S. Newell for assistance with TGA and XRD data collection and Bryan Brittan for performing the ICP-AES analyses. We are grateful for insightful discussions with Professors Richard G. Finke and Andrew K. Galwey and for the assistance provided by Dr. Ioannis Tiritiris, Dr. Nguyen Duc Van, Dr. Thomas Schölkopf, Dr. Mimoza Gjikaj, Prof. Peter C. Junk, Prof. Glen B. Deacon, Prof. Jack Passmore, Prof. Leslie Glasser, and Prof. Graham Smith in the preparation of this manuscript. We thank Argonne National Laboratory, Edwards Air Force Base (AFRL/RZSP), the U.S. National Science Foundation (Grant CHE-1362302), the Colorado State University Foundation, and the Slovene Human Resources Development and Scholarship Fund for financial support.

■ REFERENCES

(1) Peryshkov, D. V.; Popov, A. A.; Strauss, S. H. Latent Porosity in Potassium Dodecafluoro-*closo*-dodecaborate(2−). Structures and Rapid Room Temperature Interconversions of Crystalline $K_2B_{12}F_{12}$, $K_2(H_2O)_2B_{12}F_{12}$, and $K_2(H_2O)_4B_{12}F_{12}$ in the Presence of Water Vapor. *J. Am. Chem. Soc.* **2010**, *132*, 13902−13913.

(2) Peryshkov, D. V.; Strauss, S. H. $K_2B_{12}F_{12}$: A rare AX_2 structure for an ionic compound at ambient conditions. *J. Fluorine Chem.* **2010**, *131*, 1252−1256.

(3) Peryshkov, D. V.; Goreshnik, E.; Mazej, Z.; Strauss, S. H. Cocrystallization of octahedral and icosahedral fluoroanions in $K_3(AsF_6)(B_{12}F_{12})$ and $Cs_3(AsF_6)(B_{12}F_{12})$. Rare examples of salts containing fluoroanions with different shapes and charges. *J. Fluorine Chem.* **2010**, *131*, 1225−1228.

(4) Belletire, J. C.; Schneider, S.; Shackelford, S. A.; Peryshkov, D. V.; Strauss, S. H. Pairing heterocyclic cations with *closo*-dodecafluorododecaborate (2−) Synthesis of binary heterocyclium(1+) salts and a $Ag_4(heterocycle)_8^{4+}$ salt of $B_{12}F_{12}^{2-}$. *J. Fluorine Chem.* **2011**, *132*, 925−936.

(5) Peryshkov, D. V.; Bukovsky, E. V.; Folsom, T. C.; Strauss, S. H. Solid-state solvation and anion packing patterns in X-ray structures of crystalline $K_2(solv)_nB_{12}F_{12}$ (solv = H_2O_2(aq), CH_3OH, CH_3NO_2, and CH_3CN). *Polyhedron* **2013**, *58*, 197−205.

(6) Peryshkov, D. V.; Friedemann, R.; Goreshnik, E.; Mazej, Z.; Seppelt, K.; Strauss, S. H. Anion packing, hole filling, and HF solvation in $A_2(HF)_nB_{12}F_{12}$ and $K_2(HF)TiF_6$ (A = K, Cs). *J. Fluorine Chem.* **2013**, *145*, 118−127.

(7) Bukovsky, E. V.; Peryshkov, D. V.; Wu, H.; Zhou, W.; Tang, W. S.; Jones, W. M.; Stavila, V.; Udovic, T. J.; Strauss, S. H. Comparison of the Coordination of $B_{12}F_{12}^{2-}$, $B_{12}Cl_{12}^{2-}$, and $B_{12}H_{12}^{2-}$ to Na^+ in the Solid State: Crystal Structures and Thermal Behavior of $Na_2(B_{12}F_{12})$, $Na_2(H_2O)_4(B_{12}F_{12})$, $Na_2(B_{12}Cl_{12})$, and $Na_2(H_2O)_6(B_{12}Cl_{12})$. *Inorg. Chem.* **2017**, *56*, 4369−4379.

(8) Donkers, P. A. J.; Pel, L.; Adan, O. C. G. Dehydration/hydration of granular beds for thermal storage applications: A combined NMR and temperature study. *Int. J. Heat Mass Transfer* **2017**, *105*, 826−830.

(9) Rajniak, P.; Soós, M.; Yang, R. T. Unified Network Model for Adsorption−Desorption in Systems with Hysteresis. *AIChE J.* **1999**, *45*, 735−750.

(10) Sohn, H. Y. The Influence of Chemical Equilibrium on Fluid-Solid Reaction Rates and the Falsification of Activation Energy. *Metall. Mater. Trans. B* **2004**, *35*, 121−131.

(11) Nakashima, Y.; Mitsumori, F. H_2O self-diffusion restricted by clay platelets with immobilized bound H_2O layers: PGSE NMR study of water-rich saponite gels. *Appl. Clay Sci.* **2005**, *28*, 209−221.

(12) Schampera, B.; Dultz, S. Determination of diffusive transport in HDPy-montmorillonite by H_2O-D_2O exchange using *in situ* ATR-FTIR spectroscopy. *Clay Miner.* **2009**, *44*, 249−266.

(13) Ladshaw, A.; Yiacoumi, S.; Tsouris, C.; DePaoli, D. Generalized gas−solid adsorption modeling: Single-component equilibria. *Fluid Phase Equilib.* **2015**, *388*, 169−181.

(14) Jänchen, J.; Ackermann, D.; Stach, H.; Brösicke, W. Studies of the water adsorption on zeolites and modified mesoporous materials for seasonal storage of solar heat. *Sol. Energy* **2004**, *76*, 339−344.

(15) Glasser, L.; Jones, F. Systematic Thermodynamics of Hydration (and of Solvation) of Inorganic Solids. *Inorg. Chem.* **2009**, *48*, 1661−1665.

(16) van Essen, V. M.; Zondag, H. A.; Gores, J. C.; Bleijendaal, L. P. J.; Bakker, M.; Schuitema, R.; van Helden, W. G. J.; He, Z.; Rindt, C. C. M. Characterization of $MgSO_4$ Hydrate for Thermochemical Seasonal Heat Storage. *J. Sol. Energy Eng.* **2009**, *131*, 041014.

(17) Posern, K.; Linnow, K.; Niermann, M.; Kaps, C.; Steiger, M. Thermochemical investigation of the water uptake behavior of $MgSO_4$ hydrates in host materials with different pore size. *Thermochim. Acta* **2015**, *611*, 1−9.

(18) Laidig, K. E.; Speers, P.; Streitwieser, A. Complexation of Li^+, Na^+, and K^+ by water and ammonia. *Coord. Chem. Rev.* **2000**, *197*, 125−139.

DOI: 10.1021/acs.inorgchem.7b02081
Inorg. Chem. 2017, 56, 12023−12041

(19) Śmiechowski, M.; Gojło, E.; Stangret, J. Ionic Hydration in $LiPF_6$, $NaPF_6$, and KPF_6 Aqueous Solutions Derived from Infrared HDO Spectra. *J. Phys. Chem. B* **2004**, *108*, 15938−15943.
(20) Persson, I.; Nilsson, K. B. Coordination Chemistry of the Solvated Silver(I) Ion in the Oxygen Donor Solvents Water, Dimethyl Sulfoxide, and *N,N′*-Dimethylpropyleneurea. *Inorg. Chem.* **2006**, *45*, 7428−7434.
(21) Fulton, J. L.; Kathmann, S. M.; Schenter, G. K.; Balasubramanian, M. Hydrated Structure of Ag(I) Ion from Symmetry-Dependent, K- and L-Edge XAFS Multiple Scattering and Molecular Dynamics Simulations. *J. Phys. Chem. A* **2009**, *113*, 13976−13984.
(22) Li, B.; Zang, S.-Q.; Li, H.-Y.; Wu, Y.-J.; Mak, T. C. W. Diverse intermolecular interactions in silver(I)-organic frameworks constructed with flexible supramolecular synthons. *J. Organomet. Chem.* **2012**, *708*−*709*, 112−117.
(23) Hunger, J.; Beta, I. A.; Böhlig, H.; Ling, C.; Jobic, H.; Hunger, B. Adsorption Structures of Water in NaX Studied by DRIFT Spectroscopy and Neutron Powder Diffraction. *J. Phys. Chem. B* **2006**, *110*, 342−353.
(24) Navrotsky, A.; Trofymluk, O.; Levchenko, A. A. Thermochemistry of Microporous and Mesoporous Materials. *Chem. Rev.* **2009**, *109*, 3885−3902.
(25) Seoung, D.; Lee, Y.; Kao, C.-C.; Vogt, T.; Lee, Y. Super-Hydrated Zeolites: Pressure-Induced Hydration in Natrolites. *Chem. - Eur. J.* **2013**, *19*, 10876−10883.
(26) Shin, J.; Bhange, D. S.; Park, M. B.; Hong, S. B. Structural characterization of various alkali cation forms of synthetic aluminosilicate natrolites. *Microporous Mesoporous Mater.* **2015**, *210*, 20−25 and references cited therein.
(27) Sakurai, H.; Ihara, Y.; Takada, K. Superconductivity of cobalt oxide hydrate, $Na_x(H_3O)_zCoO_2{\cdot}yH_2O$. *Phys. C* **2015**, *514*, 378−397 and references cited therein.
(28) Udovic, T. J.; Matsuo, M.; Unemoto, A.; Verdal, N.; Stavila, V.; Skripov, A. V.; Rush, J. J.; Takamura, H.; Orimo, S.-I. Sodium superionic conduction in $Na_2B_{12}H_{12}$. *Chem. Commun.* **2014**, *50*, 3750−3752.
(29) Udovic, T. J.; Matsuo, M.; Tang, W. S.; Wu, H.; Stavila, V.; Soloninin, A. V.; Skoryunov, R. V.; Babanova, O. A.; Skripov, A. V.; Rush, J. J.; Unemoto, A.; Takamura, H.; Orimo, S.-I. Exceptional Superionic Conductivity in Disordered Sodium Decahydro-*closo*-decaborate. *Adv. Mater.* **2014**, *26*, 7622−7626.
(30) Sagua, A.; Rivera, A.; León, C.; Santamaría, J.; Sanz, J.; Morán, E. High ionic conductivity of hydrated $Li_{0.5}FeOCl$. *Solid State Ionics* **2006**, *177*, 1099−1104.
(31) Saeed, Y.; Singh, N.; Schwingenschlögl, U. Superior thermoelectric response in the 3R phases of hydrated Na_xRhO_2. *Sci. Rep.* **2015**, *4*, 4390.
(32) Raijada, D.; Müllertz, A.; Cornett, C.; Munk, T.; Sonnergaard, J.; Rantanen, J. Miniaturized Approach for Excipient Selection During the Development of Oral Solid Dosage Form. *J. Pharm. Sci.* **2014**, *103*, 900−908 and references cited therein.
(33) Zhang, X.; Yin, Q.; Du, W.; Gong, J.; Bao, Y.; Zhang, M.; Hou, B.; Hao, H. Phase Transformation between Anhydrate and Monohydrate of Sodium Dehydroacetate. *Ind. Eng. Chem. Res.* **2015**, *54*, 3438−3444.
(34) Sovago, I.; Wang, W.; Qiu, D.; Raijada, D.; Rantanen, J.; Grohganz, H.; Rades, T.; Bond, A. D.; Löbmann, K. Properties of the Sodium Naproxen-Lactose-Tetrahydrate Co-Crystal upon Processing and Storage. *Molecules* **2016**, *21*, 509 (pp 1-13) and references cited therein.
(35) Ivanov, S. V.; Casteel, W. J., Jr.; Bailey, W. H., III High purity lithium polyhalogenated boron cluster salts useful in lithium batteries. U.S. Patent 7,465,517.
(36) Arai, J.; Matsuo, A.; Fujisaki, T.; Ozawa, K. A novel high temperature stable lithium salt ($Li_2B_{12}F_{12}$) for lithium ion batteries. *J. Power Sources* **2009**, *193*, 851−854.
(37) Hayamizu, K.; Matsuo, A.; Arai, J. A Divalent Lithium Salt $Li_2B_{12}F_{12}$ Dissolved in Propylene Carbonate Studied by NMR Methods. *J. Electrochem. Soc.* **2009**, *156*, A744−A750.
(38) GirishKumar, G.; Bailey, W. H., III; Peterson, B. K.; Casteel, W. J., Jr. Electrochemical and Spectroscopic Investigations of the Overcharge Behavior of StabiLife Electrolyte Salts in Lithium-Ion Batteries. *J. Electrochem. Soc.* **2011**, *158*, A146−A153.
(39) Xu, K. Electrolytes and Interphases in Li-Ion Batteries and Beyond. *Chem. Rev.* **2014**, *114*, 11503−11618.
(40) Shriver, D. F.; Drezdzon, M. A. *The Manipulation of Air-Sensitive Compounds*; Wiley-Interscience: New York, 1986.
(41) Peryshkov, D. V.; Popov, A. A.; Strauss, S. H. Direct Perfluorination of $K_2B_{12}H_{12}$ in Acetonitrile Occurs at the Gas Bubble-Solution Interface and Is Inhibited by HF. Experimental and DFT Study of Inhibition by Protic Acids and Soft, Polarizable Anions. *J. Am. Chem. Soc.* **2009**, *131*, 18393−18403.
(42) Peryshkov, D. V.; Bukovsky, E. V.; Strauss, S. H. Efficient Perfluorination of $K_2B_{12}H_{12}$ in Neutral Acetonitrile. In *Efficient Preparation of Fluorine Compounds*; Roesky, H., Ed.; Wiley: New York, 2012; pp 16−18.
(43) Peryshkov, D. V.; Strauss, S. H. Exceptional Structural Compliance of the $B_{12}F_{12}^{2-}$ Superweak Anion. *Inorg. Chem.* **2017**, *56*, 4072−4083.
(44) Peryshkov, D. V. Direct Fluorination of $K_2B_{12}F_{12}$ and Synthesis and Characterization of Metal Salts of $B_{12}F_{12}^{2-}$. Ph.D. Dissertation, Colorado State University, Fort Collins, CO, 2011.
(45) Malischewski, M.; Peryshkov, D. V.; Bukovsky, E. V.; Seppelt, K.; Strauss, S. H. Structures of $M_2(SO_2)_6B_{12}F_{12}$ (M = Ag or K) and $Ag_2(H_2O)_4B_{12}F_{12}$: Comparison of the Coordination of SO_2 versus H_2O and of $B_{12}F_{12}^{2-}$ versus Other Weakly Coordinating Anions to Metal Ions in the Solid State. *Inorg. Chem.* **2016**, *55*, 12254−12262.
(46) Brese, N. E.; O'Keeffe, M. Bond-Valence Parameters for Solids. *Acta Crystallogr., Sect. B: Struct. Sci.* **1991**, *47*, 192−197.
(47) Giannozzi, P.; et al. QUANTUM ESPRESSO: A Modular and Open-Source Software Project for Quantum Simulations of Materials. *J. Phys.: Condens. Matter* **2009**, *21*, 395502.
(48) Khaliullin, R. S.; Khisamov, B. A. $KCs(ClO_4)_2$. *High Energy Chem.* **1996**, *30*, 394−396.
(49) Khranenko, S. P.; Baidina, I. A.; Kuratieva, N. V.; Gromilov, S. A. $KCs[Pd(NO_3)_4]{\cdot}0.5H_2O$. *J. Struct. Chem.* **2009**, *50*, 166−169.
(50) Sieroń, L.; Bukowska-Strzyżewska, M.; Cygański, A.; Turek, A. $KCs_2[Bi(SCN)_6]$. *Polyhedron* **1996**, *15*, 3923−3931.
(51) Popov, D. Y.; Kavun, V. Y.; Gerasimenko, A. V.; Sergienko, V. I.; Antokhina, T. F. Crystal structures of $LiCsTiF_6$ and Cs_2TiF_6 and internal mobility of complex anions. *Russ. J. Coord. Chem.* **2002**, *28*, 19−24.
(52) Nickels, E. A.; Jones, M. O.; David, W. I. F.; Johnson, S. R.; Lowton, R. L.; Sommariva, M.; Edwards, P. P. Tuning the Decomposition Temperature in Complex Hydrides: Synthesis of a Mixed Alkali Metal Borohydride. *Angew. Chem., Int. Ed.* **2008**, *47*, 2817−2819.
(53) Reckeweg, O.; DiSalvo, F. J. Synthesis and single-crystal structure of the pseudo-ternary compounds $LiA[N(CN)_2]_2$ (A = K or Rb). *Z. Naturforsch., B: J. Chem. Sci.* **2016**, *71*, 157−160.
(54) Reckeweg, O.; DiSalvo, F. J. The first pseudo-ternary thiocyanate containing two alkali metals - synthesis and single-crystal structure of $LiK_2[SCN]_3$. *Z. Naturforsch., B: J. Chem. Sci.* **2016**, *71*, 161−164.
(55) Fischer, J.; Krämer, V. Crystal Structure of $KNaSiF_6$. *Mater. Res. Bull.* **1991**, *26*, 925−930.
(56) Gjikaj, M.; Wu, P.; Brockner, W. New Quaternary Alkali-Metal Hypodiphosphate Hydrates: Preparation, Crystal Structure, Vibrational Spectrum, and Thermal Behavior of $K_4P_2O_6{\cdot}8H_2O$ and $Na_2K_2P_2O_6{\cdot}8H_2O$ in Comparison to $Na_4P_2O_6{\cdot}10H_2O$. *Z. Anorg. Allg. Chem.* **2012**, *638*, 2144−2149.
(57) Massa, W.; Babel, D. Crystal Structure and Bonding in Transition-Metal Fluoro Compounds. *Chem. Rev.* **1988**, *88*, 275−296 and references cited therein.

DOI: 10.1021/acs.inorgchem.7b02081
Inorg. Chem. 2017, 56, 12023−12041

(58) Hansen, B. R. S.; Paskevicius, M.; Li, H.-W.; Akiba, E.; Jensen, T. R. Metal boranes: Progress and applications. *Coord. Chem. Rev.* **2016**, *323*, 60−70.
(59) Jenne, C.; Kirsch, C. Alkoxy substituted halogenated *closo*-dodecaborates as anions for ionic liquids. *Dalton Trans.* **2015**, *44*, 13119−13124.
(60) Mascal, M.; Infantes, L.; Chisholm, J. Water Oligomers in Crystal Hydrates-What's News and What Isn't. *Angew. Chem., Int. Ed.* **2006**, *45*, 32−36.
(61) Wang, Y.; Bowman, J. M. Calculations of the IR spectra of bend fundamentals of $(H_2O)_{n=3,4,5}$ using the WHBB_2 potential and dipole moment surfaces. *Phys. Chem. Chem. Phys.* **2016**, *18*, 24057−24062 and references cited therein.
(62) Yousufuddin, M.; Her, J.-H.; Zhou, W.; Jalisatgi, S. S.; Udovic, T. J. Crystal structure, neutron vibrational spectroscopy, and DFT calculations of $Li_2B_{12}H_{12}\cdot 4H_2O$. *Inorg. Chim. Acta* **2009**, *362*, 3155−3158.
(63) Gaivoronskaya, K. A.; Gerasimenko, A. V.; Didenko, N. A.; Slobodyuk, A. B.; Kavun, V. Y. $Li_2Mg(ZrF_6)_2\cdot 4H_2O$: Synthesis, X-ray crystallographic, thermal, and MAS NMR study. *Russ. J. Inorg. Chem.* **2013**, *58*, 189−196.
(64) Loss, S.; Röhr, C. Lithium Hexafluoroarsenate Monohydrate, $LiAsF_6\cdot H_2O$. *Acta Crystallogr., Sect. C: Cryst. Struct. Commun.* **1998**, *54*, 567−569.
(65) Shchegoleva, T. M.; Iskhakova, L. D.; Trunov, V. K. Crystal structure of $LiBF_4(H_2O)$. *Kristallografiya* **1986**, *31*, 1076−1080.
(66) Marseglia, E. A.; Brown, I. D. Lithium hexafluorotitanate dihydrate and lithium hexafluorostannate dihydrate. *Acta Crystallogr., Sect. B: Struct. Crystallogr. Cryst. Chem.* **1973**, *29*, 1352−1354.
(67) Wells, A. F. *Structural Inorganic Chemistry*, 5th ed.; Oxford University Press: Oxford, U.K., 1984; p 149.
(68) Shannon, R. D. Revised Effective Ionic-Radii and Systematic Study of Interatomic Distances in Halides and Chalcogenides. *Acta Crystallogr., Sect. A: Cryst. Phys., Diffr., Theor. Gen. Crystallogr.* **1976**, *32*, 751−767.
(69) Tiritiris, I.; Schleid, T. Investigations on the Crystal Structure of Lithium Dodecahydro-*closo*-dodecaborate from Aqueous Solution: $Li_2(H_2O)_7[B_{12}H_{12}]$. *Z. Anorg. Allg. Chem.* **2002**, *628*, 1411−1418.
(70) Tiritiris, I. Untersuchungen zu Reaktivität, Aufbau und struktureller Dynamik von salzartigen *closo*-Dodekaboraten. Ph.D. Dissertation, Universität Stuttgart, Stuttgart, Germany, 2004.
(71) Steyl, G. Tetraaqualithium(I) bis(tropolonato-$\kappa^2 O,O'$)lithate(I). *Acta Crystallogr., Sect. E: Struct. Rep. Online* **2007**, *63*, m2343.
(72) Touboul, M.; Bétourné, E.; Nowogrocki, G. Crystal structure and Dehydration Process of $Li(H_2O)_4(B(OH)_4)\cdot 2H_2O$. *J. Solid State Chem.* **1995**, *115*, 549−553.
(73) Raabe, I.; Wagner, K.; Santiso-Quiñones, G.; Krossing, I. Snapshots of the Hydrolysis of the Lithium Alkoxide $[Li\{OC(CF_3)_3\}]_4$. *Z. Anorg. Allg. Chem.* **2009**, *635*, 513−517.
(74) Decken, A.; Le Blanc, F.; Passmore, J. Lithium hexafluoroarsenate(V) trihydrate. FIZ Karlsruhe ICSD 416608 (deposited as a Private Communication), 2009.
(75) Lejaeghere, K.; et al. Reproducibility in density functional theory calculations of solids. *Science* **2016**, *351*, 3001−3007.
(76) Waldner, P.; Ipser, H. The nonstoichiometric ζ-Ni_2In phase with $B8_2$-structure: thermodynamic modeling. *Intermetallics* **2002**, *10*, 485−491 and references cited therein.
(77) Glasser, L. Thermodynamics of Inorganic Hydration and of Humidity Control, with an Extensive Database of Salt Hydrate Pairs. *J. Chem. Eng. Data* **2014**, *59*, 526−530.
(78) Glasser, L.; Jenkins, H. D. B. The Thermodynamic *Solvate* Difference Rule: Solvation Parameters and Their Use in Interpretation of the Role of Bound Solvent in Condensed-Phase Solvates. *Inorg. Chem.* **2007**, *46*, 9768−9778.
(79) Jenkins, H. D. B.; Glasser, L. Ionic Hydrates, $M_pX_q\cdot nH_2O$: Lattice Energy and Standard Enthalpy of Formation Estimation. *Inorg. Chem.* **2002**, *41*, 4378−4388.
(80) Jenkins, H. D. B.; Roobottom, H. K.; Passmore, J.; Glasser, L. Relationships among Ionic Lattice Energies, Molecular (Formula Unit) Volumes, and Thermochemical Radii. *Inorg. Chem.* **1999**, *38*, 3609−3620.
(81) Ahmed, I. A.; Kastner, G.; Reuter, H.; Schultze, D. Coordination chemistry of tin Part III. The crystal structure and thermal behavior of dipotassium dimethyl-tetrafluoro-stannate dihydrate, $K_2[(CH_3)_2SnF_4]\cdot 2H_2O$. *J. Organomet. Chem.* **2002**, *649*, 147−151.
(82) de Kozak, A.; Gredin, P.; Pierrard, A.; Renaudin, J. The crystal structure of a new form of the potassium pentafluoroaluminate hydrate, $K_2AlF_5\cdot H_2O$, and of its dehydrate, K_2AlF_5. *J. Fluorine Chem.* **1996**, *77*, 39−44.
(83) Pitt, M. P.; Paskevicius, M.; Brown, D. H.; Sheppard, D. A.; Buckley, C. E. Thermal Stability of $Li_2B_{12}H_{12}$ and its Role in the Decomposition of $LiBH_4$. *J. Am. Chem. Soc.* **2013**, *135*, 6930−6941.
(84) Touboul, M.; Bétourné, E. Dehydration process of lithium borates. *Solid State Ionics* **1996**, *84*, 189−197.
(85) Li, P.; Liu, Z. Synthesis, Structure and Thermodynamic Property of a New Lithium Borate: $Li_4[B_8O_{13}(OH)_2]\cdot 3H_2O$. *Chin. J. Chem.* **2012**, *30*, 847−853.
(86) Finney, E. E.; Finke, R. G. Is There a Minimal Chemical Mechanism Underlying Classical Avrami-Erofe'ev Treatments of Phase-Transformation Kinetic Data. *Chem. Mater.* **2009**, *21*, 4692−4705.
(87) Dill, E. D.; Folmer, J. C. W.; Martin, J. D. Crystal Growth Simulations to Establish Phyically Relevant Kinetic Paramters from the Empirical Kolmogorov−Johnson−Mehl−Avrami Model. *Chem. Mater.* **2013**, *25*, 3941−3951.
(88) Galwey, A. K. Structure and order in thermal dehydrations of crystalline solids. *Thermochim. Acta* **2000**, *355*, 181−238.
(89) Galwey, A. K. What Can We Learn About the Mechanisms of Thermal Decompositions of Solids from Kinetic Measurements. *J. Therm. Anal. Calorim.* **2008**, *92*, 967−983.
(90) Koga, N.; Tanaka, H. A physico-geometric approach to the kinetics of solid-state reactions as exemplified by the thermal dehydration and decomposition of inorganic solids. *Thermochim. Acta* **2002**, *388*, 41−61.
(91) Noisong, P.; Danvirutai, C. Kinetics and Mechanism of Thermal Dehydration of $KMnPO_4\cdot H_2O$ in a Nitrogen Atmosphere. *Ind. Eng. Chem. Res.* **2010**, *49*, 3146−3151.
(92) Mianowski, A.; Tomaszewicz, M.; Siudyga, T.; Radko, T. Estimation of kinetic parameters based on finite time of reaction/process: thermogravimetric studies at isothermal and dynamic conditions. *React. Kinet., Mech. Catal.* **2014**, *111*, 45−69.
(93) Galwey, A. K. Solid state reaction kinetics, mechanisms and catalysis: a retrospective rational review. *React. Kinet., Mech. Catal.* **2015**, *114*, 1−29.
(94) Galwey, A. K. Is the science of thermal analysis kinetics based on solid foundations? A literature appraisal. *Thermochim. Acta* **2004**, *413*, 139−183.
(95) Brown, M. E. *Introduction to thermal analysis*; Kluwer Academic: Dordrecht, The Netherlands, 2001.
(96) Gjikaj, M.; Ehrhardt, C. New Hexachalcogeno−Hypodiphosphates of the Alkali Metals: Synthesis, Crystal Structure and Vibrational Spectra of the Hexathiodiphosphate(IV) Hydrates $K_4[P_2S_6]\cdot 4H_2O$, $Rb_4[P_2S_6]\cdot 6H_2O$, and $Cs_4[P_2S_6]\cdot 6H_2O$. *Z. Anorg. Allg. Chem.* **2007**, *633*, 1048−1054.
(97) Kuhn, A.; Eger, R.; Nuss, J.; Lotsch, B. V. Synthesis and Structural Characterization of the Alkali Thiophosphates $Na_2P_2S_6$, $Na_4P_2S_6$, $K_4P_2S_6$, and $Rb_4P_2S_6$. *Z. Anorg. Allg. Chem.* **2014**, *640*, 689−692.
(98) Elding, L. I.; Oskarsson, A. A Tetranitrato Complex of Platinum(I1). Synthesis and Crystal Structure of $K_2[Pt(NO_3)_4\cdot 1/2H_2O$. *Inorg. Chim. Acta* **1985**, *103*, 127−131.
(99) Amalvy, J. L.; Varetti, E. L.; Aymonino, P. J. TGA-DTA and Infrared Spectra of Potassium Nitroprusside Dihydrate: $K_2[Fe(CN)_5NO]\cdot 2H_2O$. *J. Phys. Chem. Solids* **1985**, *46*, 1153−1161.
(100) Zhao, Y.; Pan, S.; Li, F.; Wang, Y.; Fan, X.; Dong, X.; Jia, D.; Guo, J.; Zhou, Z. Synthesis, structure, and properties of a novel hydrated borate $Rb_4[B_4O_5(OH)_4]_2\cdot 3H_2O$. *Solid State Sci.* **2011**, *13*, 82−87.

DOI: 10.1021/acs.inorgchem.7b02081
Inorg. Chem. 2017, 56, 12023−12041

(101) Stöger, B.; Weil, M. The isotypic hydrogen phosphate and arsenate dihydrates $M_2HXO_4{\cdot}2H_2O$ (M = Rb, Cs; X = P, As). *Acta Crystallogr., Sect. C: Struct. Chem.* **2014**, *70*, 7−11.

(102) Soria, D. B.; Piro, O. E.; Castellano, E. E.; Aymonino, P. J. Crystal and molecular structure determination, TGA, DTA, and infrared and Raman spectra of rubidium nitroprusside monohydrate, $Rb_2[Fe(CN)_5NO]{\cdot}H_2O$. *J. Chem. Crystallogr.* **1999**, *29*, 75−80.

(103) Sotani, N.; Miyazaki, T.; Eda, K.; Hatayama, F. Preparation of hydrated rubidium molybdenum bronze from hydrated sodium molybdenum bronze by ion exchange, and its characterization and thermal decomposition. *J. Mater. Chem.* **1997**, *7*, 2253−2258.

(104) Kruszynski, R.; Sieranski, T.; Bilinska, A.; Bernat, T.; Czubacka, E. Alkali metal halogenides coordination compounds with hexamethylenetetramine. *Struct. Chem.* **2012**, *23*, 1643−1656.

(105) Deacon, G. B.; Forsyth, C. M.; Greenhill, N. B.; Junk, P. C.; Wang, J. Coordination Polymers of Increasing Complexity Derived from Alkali Metal Cations and (4-Amino-1-hydroxybutylidine)-1,1-bisphosphonic Acid (Alendronic Acid): The Competitive Influences of Coordination and Supramolecular Interactions. *Cryst. Growth Des.* **2015**, *15*, 4646−4662.

(106) Hartl, H.; Pickhard, F.; Emmerling, F.; Röhr, C. Rubidium und Caesium Compounds with the Isopolyanion $[Ta_6O_{19}]^{8-}$ − Synthesis, Crystal Structures, Thermogravimetric and Vibrational Spectroscopic Analysis of the Oxotantalates $A_8[Ta_6O_{19}]{\cdot}nH_2O$ (A = Rb, Cs; n = 0, 4, 14). *Z. Anorg. Allg. Chem.* **2001**, *627*, 2630−2638.

(107) Srinivasan, B. R.; Morajkar, S. M.; Khandolkar, S. S.; Näther, C.; Bensch, W. Synthesis, structure and properties of a hexarubidium heptamolybdate with bridging aqua ligands. *Indian J. Chem.* **2017**, *56A*, 601−609.

(108) Chernorukov, N. G.; Nipruk, O. V.; Kostrova, E. L. Cesium Uranate $Cs_3U_{12}O_{31}(OH)_{13}{\cdot}3H_2O$: Synthesis and Characterization. *Russ. J. Inorg. Chem.* **2015**, *60*, 1329−1332.

(109) Lavrova, G. V.; Bulina, N. V.; Min'kov, V. S.; Matvienko, A. A. Structure and Thermal Decomposition of $Cs_2HPO_4{\cdot}2H_2O$. *Russ. J. Inorg. Chem.* **2016**, *61*, 284−290.

(110) Bennour, R.; Rogez, J.; Mathieu, J. C.; Caranoni, C.; Thomas, P.; Zineddine, H. Cesium silicon oxide hydrates − thermal behavior in the temperature range 290−1380 K − identification by X-ray powder diffraction patterns. *Eur. J. Solid State Inorg. Chem.* **1997**, *34*, 607−618.

(111) Touboul, M.; Penin, N.; Nowogrocki, G. Crystal Structure and Thermal Behavior of $Cs_2[B_4O_5(OH)_4]3H_2O$. *J. Solid State Chem.* **1999**, *143*, 260−265.

(112) Vergara, M. M.; Varetti, E. L. Thermal Behavior and Vibrational Spectra of Cesium Nitroprusside Monohydrate, $Cs_2[Fe(CN)_5)NO]{\cdot}H_2O$. *J. Phys. Chem. Solids* **1987**, *48*, 13−19.

(113) Vergara, M. M.; Varetti, E. L.; Rigotti, G.; Navaza, A. The Crystalline and Molecular Structure and the Vibrational Spectra of Anhydrous Cesium Nitroprusside. *J. Phys. Chem. Solids* **1989**, *50*, 951−956.

(114) Tiritiris, I.; Schleid, T. The dodecahydro-*closo*-dodecaborates $M_2[B_{12}H_{12}]$ of the heavy alkali metals ($M = K^+, Rb^+, NH_4^+, Cs^+$) and their formal iodide adducts $M_3I[B_{12}H_{12}]$ ($MI{\cdot}M_2[B_{12}H_{12}]$). *Z. Anorg. Allg. Chem.* **2003**, *629*, 1390−1402.

(115) Schölkopf, T.; Van, N.-C.; Schleid, T. $Rb_2[B_{12}(OH)_{12}]{\cdot}2H_2O$ and $Rb_2[B_{12}(OH)_{12}]{\cdot}2H_2O_2$: Hydrate and perhydrolate of rubidium dodecahydroxo-closo-dodecaborate. *Inorg. Chim. Acta* **2011**, *374*, 181−186.

(116) Peymann, T.; Knobler, C. B.; Khan, S. I.; Hawthorne, M. F. Dodecahydroxy-*closo*-dodecaborate(2−). *J. Am. Chem. Soc.* **2001**, *123*, 2182−2185.

(117) Tiritiris, I.; Schleid, T. The Crystal Structures of the Dicesium Dodeachalogeno-*closo*-Dodecaborates $Cs_2[B_{12}X_{12}]$ (X = Cl, Br, I) and their Hydrates. *Z. Anorg. Allg. Chem.* **2004**, *630*, 1555−1563.

(118) Elding, L. I.; Noren, B.; Oskarsson, A. Synthesis and Crystal Structure of Potassium Tetranitrito Palladate(II). *Inorg. Chim. Acta* **1986**, *114*, 71−74.

(119) Castellano, E. E.; Rivero, B. E.; Piro, O. E.; Amalvy, J. L. Structures of Potassium Nitroprusside 2.5 and 0.8 Hydrates. *Acta Crystallogr., Sect. C: Cryst. Struct. Commun.* **1989**, *45*, 1207−1210.

(120) Soria, D. B.; Amalvy, J. L.; Piro, O. E.; Castellano, E. E.; Aymonino, P. J. Crystal and molecular structure determination, TGA, DTA, and infrared and Raman spectra of rubidium nitroprusside, $Rb_2[Fe(CN)_5NO]$. *J. Chem. Crystallogr.* **1996**, *26*, 325−330.

(121) Tiritiris, I.; Schleid, T.; Müller, K. Solid-State NMR Studies on Ionic *closo*-Dodecaborates. *Appl. Magn. Reson.* **2007**, *32*, 459−481.

(122) Skripov, A. V.; Babanova, O. A.; Soloninin, A. V.; Stavila, V.; Verdal, N.; Udovic, T. J.; Rush, J. J. Nuclear Magnetic Resonance Study of Atomic Motion in $A_2B_{12}H_{12}$ (A = Na, K, Rb, Cs): Anion Reorientations and Na^+ Mobility. *J. Phys. Chem. C* **2013**, *117*, 25961−25968.

(123) Verdal, N.; Udovic, T. J.; Rush, J. J.; Cappelletti, R. L.; Zhou, W. Reorientational Dynamics of the Dodecahydro-*closo*-dodecaborate Anion in $Cs_2B_{12}H_{12}$. *J. Phys. Chem. A* **2011**, *115*, 2933−2938.

(124) Verdal, N.; Udovic, T. J.; Stavila, V.; Tang, W. S.; Rush, J. J.; Skripov, A. V. Anion Reorientations in the Superionic Conducting Phase of $Na_2B_{12}H_{12}$. *J. Phys. Chem. C* **2014**, *118*, 17483−17489.

(125) Verdal, N.; Her, J.-H.; Stavila, V.; Soloninin, A. V.; Babanova, O. A.; Skripov, A. V.; Udovic, T. J.; Rush, J. J. Complex high-temperature phase transitions in $Li_2B_{12}H_{12}$ and $Na_2B_{12}H_{12}$. *J. Solid State Chem.* **2014**, *212*, 81−91.

(126) Kiselev, V. D.; Miller, J. G. Experimental Proof That the Diels−Alder Reaction of Tetracyanoethylene with 9,10-Dimethylanthracene Passes through Formation of a Complex between the Reactants. *J. Am. Chem. Soc.* **1975**, *97*, 4036−4039.

(127) Fukuzumi, S.; Endo, Y.; Imahori, H. A Negative Temperature Dependence of the Electron Self-Exchange Rates of Zinc Porphyrin π Radical Cations. *J. Am. Chem. Soc.* **2002**, *124*, 10974−10975.

(128) Zhu, X.-Q.; Zhang, J.-Y.; Cheng, J.-P. Negative Kinetic Temperature Effect on the Hydride Transfer from NADH Analogue BNAH to the Radical Cation of N-Benzylphenothiazine in Acetonitrile. *J. Org. Chem.* **2006**, *71*, 7007−7015.

(129) Wang, L.; Moss, R. A.; Krogh-Jespersen, K. Complexes and Negative Activation Energies in Arylhalocarbene/Alkene Additions: Activation Parameter Dependence on Alkane Solvent Chain Length. *J. Org. Chem.* **2017**, *82*, 4216−4225.

(130) Cunningham, D. A. H.; Vogel, W.; Haruta, M. Negative activation energies in CO oxidation over an icosahedral $Au/Mg(OH)_2$ catalyst. *Catal. Lett.* **1999**, *63*, 43−47.

(131) Valverde, J. M. On the negative activation energy for limestone calcination at high temperatures nearby equilibrium. *Chem. Eng. Sci.* **2015**, *132*, 169−177.

(132) Kwon, J. H.; Wilson, L. D.; Sammynaiken, R. Sorptive uptake of selenium with magnetite and its supported materials onto activated carbon. *J. Colloid Interface Sci.* **2015**, *457*, 388−397.

(133) Carrillo, A. J.; Serrano, D. P.; Pizarro, P.; Coronado, J. M. Understanding Redox Kinetics of Iron-Doped Manganese Oxides for High Temperature Thermochemical Energy Storage. *J. Phys. Chem. C* **2016**, *120*, 27800−27812.

(134) Lekgoathi, M. D. S.; Vilakazi, B. M.; Wagener, J. B.; Le Roux, J. P.; Moolman, D. Decomposition kinetics of anhydrous and moisture exposed $LiPF_6$ salts by thermogravimetry. *J. Fluorine Chem.* **2013**, *149*, 53−56.

(135) Lu, Z.; Yang, L.; Guo, Y. Thermal behavior and decomposition kinetics of six electrolyte salts by thermal analysis. *J. Power Sources* **2006**, *156*, 555−559.

(136) Zhou, Y.-A.; Zhang, X.-Y.; Nian, H.-E.; Pang, Y.-N.; Wang, H.-B. Preparation and Characterization of $LiBF_4$ by Gradient Heating Dehydration. *Acta Chim. Sin.* **2010**, *68*, 1399−1403.

(137) Han, H.-B.; Zhou, S.-S.; Zhang, D.-J.; Feng, S.-W.; Li, L.-F.; Liu, K.; Feng, W.-F.; Nie, J.; Li, H.; Huang, X.-J.; Armand, M.; Zhou, Z.-B. Lithium bis(fluorosulfonyl)imide (LiFSI) as conducting salt for nonaqueous liquid electrolytes for lithium-ion batteries: Physicochemical and electrochemical properties. *J. Power Sources* **2011**, *196*, 3623−3632.

(138) Buschmann, W. E.; Miller, J. S. Sources of Naked Divalent First-Row Metal Ions: Synthesis and Characterization of $[M^{II}(NCCH_3)_6]^{2+}$ (M = V, Cr, Mn, Fe, Co, Ni) Salts of Tetrakis[3,5-bis(trifluoromethyl)phenyl]borate. *Chem. - Eur. J.* **1998**, *4*, 1731−1737.

DOI: 10.1021/acs.inorgchem.7b02081
Inorg. Chem. 2017, 56, 12023−12041